Function of ceramide transfer protein for biogenesis and sphingolipid composition of extracellular vesicles

Simone M. Crivelli[1,2] | **Caterina Giovagnoni**[3] | **Zhihui Zhu**[1] | **Priyanka Tripathi**[1,2] | **Ahmed Elsherbini**[1] | **Zainuddin Quadri**[1,2] | **Jian Pu**[4] | **Liping Zhang**[1,2] | **Branislav Ferko**[5] | **Dusan Berkes**[5] | **Stefka D. Spassieva**[1] | **Pilar Martinez-Martinez**[3] | **Erhard Bieberich**[1,2]

[1]Department of Physiology, University of Kentucky, Lexington, Kentucky, USA

[2]Veterans Affairs Medical Center, Lexington, Kentucky, USA

[3]Department of Psychiatry and Neuropsychology, School for Mental Health and Neuroscience, Maastricht University, Maastricht, The Netherlands

[4]Department of Surgery, University of Kentucky, Lexington, Kentucky, USA

[5]Department of Organic Chemistry, Slovak University of Technology, Bratislava, Slovak Republic

Correspondence
Dr. Erhard Bieberich, Department of Physiology, University of Kentucky School of Medicine, Lexington, KY, 40506, USA.
Email: Erhard.Bieberich@uky.edu

Dr. Pilar Martinez-Martinez, Department of Psychiatry and Neuropsychology, School for Mental Health and Neuroscience, Maastricht University, Maastricht, The Netherlands
Email: p.martinez@maastrichtuniversity.nl

Pilar Martinez-Martinez and Erhard Bieberich shared senior authorship.

Abstract

The formation of extracellular vesicles (EVs) is induced by the sphingolipid ceramide. How this pathway is regulated is not entirely understood. Here, we report that the ceramide transport protein (CERT) mediates a non-vesicular transport of ceramide between the endoplasmic reticulum (ER) and the multivesicular endosome at contact sites. The process depends on the interaction of CERT's PH domain with PI4P generated by PI4KIIα at endosomes. Furthermore, a complex is formed between the START domain of CERT, which carries ceramide, and the Tsg101 protein, which is part of the endosomal sorting complex required for transport (ESCRT-I). Inhibition of ceramide biosynthesis reduces CERT-Tsg101 complex formation. Overexpression of CERT increases EV secretion while its inhibition reduces EV formation and the concentration of ceramides and sphingomyelins in EVs. In conclusion, we discovered a function of CERT in regulating the sphingolipid composition and biogenesis of EVs, which links ceramide to the ESCRT-dependent pathway.

KEYWORDS
AlphaFold2, ceramide, CERT, ER-endosome contact sites, extracellular vesicles, HPA-12, NC03, PI4P, PI4KIIIβ, PI4KIIIβ-IN-10, PI4KIIα, sphingomyelin, Tsg101

1 | INTRODUCTION

The sphingolipid ceramide is important for extracellular vesicle (EV) formation in vitro and in vivo (Dinkins et al., 2014, 2016; Menck et al., 2017; Trajkovic et al., 2008). Generation of ceramide at the plasma membrane and/or at the endosomal system

by the enzyme neutral sphingomyelinase 2 (N-SMase 2) regulates EV biogenesis (Menck et al., 2017; Trajkovic et al., 2008). By breaking down sphingomyelin (SM), N-SMase 2 increases the membrane levels of ceramide, which favours membrane budding because of its peculiar cone-shaped structure (Trajkovic et al., 2008). This process is thought to be independent of the endosomal sorting complex required for transport (ESCRT), which consist of approximately twenty proteins assembling into four complexes (ESCRT-0, -I, -II, and -III) that regulate cargo selection and biogenesis of EVs (Kenific et al., 2021). However, other enzymes in sphingolipid metabolism have been shown to regulate EV formation, such as sphingomyelin synthase 1 (SMS1) and sphingomyelin synthase 2 (SMS2) which convert ceramide into SM in the trans-Golgi and plasma membrane, respectively. When SMS1 transcription is silenced, cells increase the number of EVs by about twofold (Yuyama et al., 2012). Similarly, inhibition of SMS2 stimulates a remarkable fourfold increase of EV secretion (Yuyama et al., 2012). Therefore, the accumulation of ceramide in the trans-Golgi and plasma membrane seems to regulate EV formation without necessarily invoking the activation of N-SMase-2. How these ceramide-dependent pathways are controlled remains poorly understood. Furthermore, it is still not clear how the lipid profile of EVs is regulated. In fact, the lipid composition of EVs is not identical to the lipid profile of the donor cells (Skotland et al., 2019). Interestingly, the EV membrane is particularly enriched in sphingolipids compared to the membrane of the donor cells (Skotland et al., 2019). How the sphingolipid composition is regulated in the endosome pathway and in EVs is yet to be investigated.

The ceramide transfer protein (CERT) is an essential protein of the sphingolipid metabolism (Hanada et al., 2003; Kumagai et al., 2005; Rao et al., 2007, 2014). After ceramide is synthetized in the endoplasmic reticulum (ER), CERT extracts and relocates ceramide to the trans-Golgi where SM is synthesized (Gault et al., 2010; Mencarelli et al., 2010). There are three functional domains of CERT involved in this process. The steroidogenic acute regulatory protein (StAR)-related lipid transfer START domain binds to ceramide and very poorly to other lipids such as diacylglycerols, which structurally resemble ceramide (Kumagai et al., 2005). The pleckstrin homology domain (PH) targets phosphatidylinositol 4-monophosphate (PI4P), which is particularly enriched in the trans-Golgi (Hanada et al., 2003; Prashek et al., 2013). Finally, the two phenylalanines in an acidic tract (FFAT) motif interact with the ER-resident protein VAMP-associated protein (VAP) (Kawano et al., 2006). Pharmacological displacement of ceramide from the START domain pocket with ceramide analogues such as HPA-12, or genetic mutation and inactivation of the PH domain, rapidly reduces SM synthesis (Yamaji & Hanada, 2014; Yasuda et al., 2001). HPA-12 displaces endogenous ceramide and occupies the amphiphilic cavity of the START domain of CERT preventing ceramide to be shuttled to the trans-Golgi (Santos et al., 2014; Yasuda et al., 2001). Interestingly, Fukushima et al., proposed a model in which CERT mediates the release of EVs enriched in ceramide, under lipotoxic conditions (Fukushima et al., 2018). Furthermore, Barman et al. just recently highlighted the role of CERT in the biogenesis of a unique subset of RNA-containing EVs (Barman et al., 2022). However, it remains unknown whether CERT plays a role in the EV machinery under physiological conditions and how CERT mechanistically participates in EV biogenesis.

In this study, we show that CERT enters the endocytic pathway and is released in EVs. Translocation of CERT to the multivesicular endosome (MVE) is dependent on the interaction of CERT's PH domain with PI4P at the MVE. We also discovered that a CERT-mediated transport of ceramide from the ER to late endosomes is regulated by PI4P generated by PI4KIIα. A complex is formed between CERT and tumour susceptibility gene 101 protein (Tsg101), which is part of the ESCRT-I complex. Inhibition of ceramide synthesis in the ER by Fumonisin B1 (FB1) reduces CERT-Tsg101 complex formation. Overexpression of CERT in neuronal cells increases EV secretion while functional inhibition of CERT with the drug HPA-12 reduces EV formation and the concentration of ceramide and SM in EVs. Our data indicate a crucial role of CERT in the biogenesis and regulation of ceramide and SM levels in EVs. We also provide for the first-time evidence that CERT links ceramide to the ESCRT-dependent pathway for EV biogenesis.

2 | MATERIALS AND METHODS

2.1 | Cloning, constructs and antibodies

The human CERT (isoform 2, 1800bp, NCBI Reference Sequence: NM_NM_031361.3) and CERT$_L$ (isoform 1, 1875bp, NCBI Reference Sequence: NM_005713.3) were constructed in the pcDNA3.1 plasmid, obtaining plasmids pcDNA3.1-CERT and pcDNA3.1-CERT$_L$ respectively. CERT$_L$ was also subcloned in the pEGFP-N1 plasmid to generate full length GFP tagged CERT$_L$ plasmid (FL-CERT$_L$-GFP) with the following primers: forward CAG ATC TCG AGA TGT CGG ATA ATC AGA GCT GGA ACT CGT CG and reverse CAT GGT ACC GCG AAC AAA ATA GGC TTT CCT GCA GT. The PH deficient CERT was cloned in the pEGFP-N1 plasmid (PH-deficient CERT$_L$-GFP) with the following primers: forward CAG ATC TCG AGA TGA ATC CAG CTT GCG TCG ACA TGG CTC AAT GG and reverse CAT GGT ACC GCG AAC AAA ATA GGC TTT CCT GCA GT. For transfection, the pEGFP-N1 plasmid was used as a control vector. pcDNA3.1-CERT, pcDNA3.1-CERTL, FL-CERT$_L$-GFP or PH-deficient CERT$_L$-GFP were used for overexpression of CERT. The two isoforms, CERT and CERT$_L$, had a similar effect on EV biogenesis, which enabled us to use the two CERT isoforms interchangeably depending on the assay performed. A plas-

mid containing tdTomato-CD9 (AddGene, plasmid #58076) was used for colocalization studies at the MVE. Transfection was performed using Lipofectamine 3000 (ThermoFisher), Effectene Transfection reagent (Qiagen) or Polyethyleneimine.

The following primary antibodies were used: anti-Alix mouse IgG (1:1000, Santa Cruz, 1A12), anti-βactin mouse (1:1000, Santa Cruz, AC-15), anti-Calnexin goat IgG (1:100 for immunofluorescence (IF) Santa Cruz, C-20), anti-CD81 mouse IgG (1:100 for IF, and 1:500 for Western blotting, Santa Cruz, B-11), anti-CD81 rabbit IgG (1:100 for IF, Santa Cruz, H-121), anti-CERT rabbit IgG (1:500 for IF and 1:2500 for Western blotting, Bethyl Laboratories, A300-669A), mouse monoclonal anti-CERT$_L$ antibody (clone 3A1H9) (Mencarelli et al., 2012), anti-EEA1 mouse IgG (1:100 IF Santa Cruz, E-8), anti-Flotillin-2 mouse IgG (1:1000 for Western blotting, BD Biosciences, 610383), anti-Flotillin-1 mouse IgG (1:1000 for Western blotting, BD Transduction Laboratories, 610820), anti-GFP mouse IgG (1:1000 for Western blotting, Santa Cruz, B-2), anti-GM130 mouse IgG (1:100, BD Biosciences), anti-LAMP1 mouse IgG (1:100 IF Santa Cruz, H4A3), anti-LBPA mouse IgG (1:300 IF, Echelon Bioscience), anti-N-SMase-2 mouse (1:1000, Santa Cruz, G-6) and anti-Tsg101 mouse IgG (1:100 for IF and 1:1000 for Western blotting, Santa Cruz, C-2). The rabbit γ-immunoglobin (Jackson ImmunoResearch) was used as technical control in the PLA assay with anti-Tsg101 at a final concentration of 4 ng/μl. Secondary antibodies were Cy2-conjugated or Alexa-647 donkey anti-mouse IgG, or Cy3-conjugated donkey anti-rabbit IgG, (1:500 Jackson ImmunoResearch).

2.2 | Yeast two-hybrid analysis (Y2Hs)

Yeast two-hybrid screening was performed by Hybrigenics Services, S.A.S., Evry, France (http://www.hybrigenics-services.com). The coding sequence of the N-terminus (aa 1–116) of human CERT (NM_005713.3) was PCR-amplified and cloned into pB29 as an N-terminal fusion to LexA (CERT-Nter-LexA) and pB66 as a C-terminal fusion to the Gal4 DNA-binding domain (Gal4-CERT-Nter). The coding sequence of the C-terminus (aa 397–624) of CERT was PCR-amplified and cloned into pB27 and pB66 as a C-terminal fusion to LexA (LexA-CERT-Cter) and the Gal4 DNA-binding domain (Gal4-CERT-Cter), respectively. The constructs were checked by sequencing and used as baits to screen a random-primed human adult brain cDNA library constructed into pP6 as described previously (Bartel et al., 1993; Beranger, 1997; Kabani et al., 2000; Vojtek & Hollenberg, 1995). The clones and colonies were screened and selected as previously described (Pettersen et al., 2021). The prey fragments of the positive clones were amplified by PCR and sequenced at their 5' and 3' junctions. The resulting sequences were used to identify the corresponding interacting proteins in the GenBank database (NCBI) using a fully automated procedure. A confidence score (PBS, for Predicted Biological Score) was attributed to each interaction as previously described (Formstecher et al., 2005).

2.3 | Immunoassay for detection of the CERT-Tsg101 complex and complex modelling with AlphaFold2 in ColabFold

ELISA. Maxisorp plates (Nunc, 423501, Biolegend) were coated with 2 μg/ml of recombinant human CERT$_L$ (rCERT$_L$), produced as previously described (Crivelli et al., 2021), overnight at room temperature in 0.1 M carbonate buffer (pH 9.6), 100 μl/well. The next day plates were washed with 0.005% Tween 20 in PBS (washing buffer 200 μl/well) and blocked for 1 h at 37°C with 3% BSA in PBS 200 μl/well. Recombinant full length human Tsg101 (Origene, TP710086) was incubated for 1 h at 37°C in serial dilutions 1, 0.5, 0.25, 0.125, 0.0625, and 0.03125 μg/ml in incubation buffer composed by 0.1% BSA in washing buffer 100 μl/well. After washing, 1 μg/ml of anti-Tsg101 mouse IgG (Santa Cruz, C-2) was incubated for 1 h followed by washing and anti-mouse-HRP donkey IgG (Jackson ImmunoResearch) diluted in incubation buffer to 0.1 μg/ml. After developing with 3,3',5,5'-Tetramethylbenzidine (TMB) the absorption was measured at 450 nm within 15 min of stopping the reaction with 2M H_2SO_4 using Synergy H1 (BioTek) multi-mode microplate reader. Wells coated with 2 μg/ml Ovalbumin were used as technical control. When coating with rTsg101 (1 μg/ml, 100 μl/well) detection of rCERT$_L$ (serial dilutions 2, 1, 0.5, 0.25, 0.125, 0.062, 0.031 μg/ml) was performed with anti-CERTs rabbit IgG (Bethyl Laboratories, A300-668A, epitope 1–50) or anti-CERTs rabbit IgG (Bethyl Laboratories, A300-669A, epitope 300–350) followed by anti-rabbit-HRP donkey IgG (Jackson ImmunoResearch).

AlphaFold 2 in CoLabFold. In the open-source Google CoLabFold platform the human FASTA sequence of the START domain (Uniprot ID: |Q9Y5P4|389-618) and UEV domain of human Tsg101 (Uniprot ID: |Q99816| 2–145) were pasted in the query sequence box and the complex prediction was run with the following advance settings: msa mode: MMseqs, model type AlphaFold2-multimer, pair mode unpaired+paired and number of recycles were set to 12 as suggested (Mirdita et al., 2021). Here we report only the output of the best-ranked model. The output consists of: (1) the schematic structure coloured by polymers chain, (2) schematic structure coloured by predicted Local Distance Difference Test (pLDDT) and the predicted aligned error (PAE) (Mirdita et al., 2021). pLDDT value close to 100 (darker blue areas in pLDDT schematic structure) represent alignments with high confident prediction. Nevertheless, the PAE (or the predicted TMscore, which is derived from PAE) are better to assess the confidence of the predicted complex structure. Very low PAE score are associated with high confidence predictions (Mirdita et al., 2021). The 3D structure and the colour surface electrostatic potential of the complex were created with UCSF ChimeraX version: 1.3 (Pettersen et al., 2021).

2.4 | Animals

C57BL/6 wild type (WT) mice were bred in-house. Animals were socially housed under a 12 h light/dark cycle in individually ventilated cages. Food and water were provided ad libitum throughout the study. Neonates P0 were used to generate primary neurons as explained in the section below. HPA-12 was dissolved in ethanol and further diluted in Dulbecco's Phosphate-Buffered Saline (DPBS) without calcium and magnesium (Corning, MA, USA) to reduce ethanol concentration to 5%, which is well tolerated by mice (Gad et al., 2006). HPA-12 was administered intraperitoneally (IP) at the dose 2 μg/g animals given every 48 h. The vehicle (5% ethanol in DPBS) was used as a control. The volume injected per animal was adjusted to 0.2 ml and administered with insulin syringes. Two-month-old mice, 10 females and 10 males, were equally divided in vehicle control or HPA-12-treated group. All experiments using mice to generate primary cell cultures or drug testing were carried out according to an Animal Use Protocol approved by the Institutional Animal Care and Use Committee at the University of Kentucky.

2.5 | Cell culture

Neuro-2a (N2a) were obtained from ATCC (CCL-131™) and maintained at 37°C and 5% CO_2 atmosphere in Dulbecco's modified Eagle's medium (DMEM) (Gibco, Invitrogen, CA, USA) supplemented with 10% fetal bovine serum (FBS) (Corning, MA, USA) and 100 U/ml penicillin-streptomycin (hyClone, GE Healthcare, UT, USA). For immunocytochemistry, N2a cells were seeded on poly-L-lysine (Milipore-Sigma, MT, USA) coated coverslips at 50,000 cells/coverslip. Cells were gradually deprived of serum for 2 to 3 days to allow for differentiation into a neuronal phenotype before immunostaining.

HeLa wild (WT) and HeLa CERT-deficient (TAL-CE#14) cells (Yamaji & Hanada, 2014) were a kind gift from Prof. Kentaro Hanada, Department of Biochemistry and Cell Biology, National Institute of Infectious Diseases, Tokyo, Japan. Cells were maintained in DMEM supplemented with 10% FBS and penicillin-streptomycin.

Primary neurons were cultured from wild type neonates (P0) as previously described (Crivelli et al., 2021). In brief, the cortical area was digested with 0.25% Trypsin in HBSS (Corning, MA, USA) for 15 min at 37° C and the reaction stopped with pre-warmed plating medium, DMEM (Gibco, Invitrogen, CA, USA) containing 10% FBS and N2 supplement. Then, the cell suspension was passed through a 40 μm cell strainer, spun down, and cells seeded in plating medium for 4 h. The plating medium was replaced with Neurobasal medium supplemented with B27 supplement, Penicillin/Streptomycin, L-glutamine, and cells cultivated for 10–14 days. Every other day, half of the Neurobasal medium with supplements was replaced.

2.6 | Incubation of cells with Fumonisin B1, PI4KIIIβ-IN-10, NC03, anti-HPA-12, syn-HPA-12 and Cer 18:1/16:0

Fumonisin B1 (FB1) was purchased from Enzo Lifesciences and a stock solution (10 mM) prepared in water. FB1 was used in cells at a final concentration of 10 μM for 24 h. The compound PI4KIIIβ-IN-10 was purchased from MedChemExpress and a stock solution of 50 μM was prepared in water and stored at -20°C. PI4KIIIβ-IN-10 was used in cells at a final concentration of 25 nM for 24 h. The PI4KIIα inhibitor NC03 was purchased from Aobious and dissolved in DMSO. NC03 was used at a final concentration of 10 or 5 μM. Both HPA-12 stereoisomers were synthesized as previously reported (Santos et al., 2015) and dissolved in ethanol. anti-HPA-12 and syn-HPA-12 were added to the cells at a concentration of 4 or 8 μM for 24h. Before incubating of cells, FB1, PI4KIIIβ-IN-10, NC03 anti-HPA-12, syn-HPA-12 were diluted in DMEM phenol red-free medium (Gibco, Invitrogen, CA, USA) without serum and supplemented with L-glutamine and 100U / mL penicillin-streptomycin (hyClone, GE Healthcare, UT, USA). The solution of Cer d18:1/16:0 2% dodecane in ethanol was diluted in DMEM phenol red-free medium with supplements as listed above and 0.34 mg / mL of defatted bovine serum albumin (Sigma). Cells were incubated for 24 h with 5 μM of Cer d18:1/16:0 alone or with 8 μM of syn-HPA-12.

2.7 | Immunofluorescence labelling

N2a or neuronal cells, prepared as described above, were fixed with ice-cold 4% PFA in PBS for 10 min, permeabilized with 0.25% Triton-X in PBS for 5 min and blocked with 3% BSA in PBS for 1 h. Primary antibodies were diluted in incubation buffer 0.3% BSA in PBS at 4 °C overnight. The next day, cells were washed 3-times with PBS and incubated with secondary antibodies for 1 h at 37 °C. Coverslips were mounted using Fluoroshield supplemented with DAPI (Sigma-Aldrich) to visualize the nuclei.

Fluorescence microscopy was performed using an Eclipse Ti2-E inverted microscope system or Nikon A1R Confocal Microscope (Nikon, New York, USA). Images were processed and analyzed using Nikon NIS-Elements software equipped with a 3D deconvolution program and particle analyzer.

2.8 | Proximity ligation assay

N2a or neuronal cells were cultivated on coverslips and transfected with Lipofectamine P3000 (ThermoFisher) and tdTomato-CD9, pcDNA3.1-CERT$_L$ or FL-CERT$_L$-GFP plasmid or treated with the drugs FB1 and HPA-12. After 24 h, cells were fixed and permeabilized as described above. The primary antibodies, anti-CD81 rabbit and anti-CERT$_L$ mouse IgG or anti-Tsg101 mouse and anti-CERT rabbit IgG, were incubated overnight. Rabbit γ-immunoglobin was used as technical control. The next day, cells were washed with PLA labelling buffer prior to the PLA reaction following the manufacturer's manual (Duolink). Images obtained with only one primary antibody or using rabbit IgG and both secondary antibodies for PLA were used as negative controls to correct for background fluorescence signals. Photomicrographs were acquired in multiple planes at different depths and a maximum intensity projection was created for counting of PLA signals and DAPI staining (for cell counts) with particle analyzer of Nikon software.

2.9 | Analysis of PHdeficient-CERT$_L$-GFP and FL-CERT$_L$-GFP cell distribution

N2a cells on coverslips were transfected with PHdeficient or FL-CERT$_L$-GFP for 24–48 h with Effectene Transfection reagent (Qiagen). Then, cells were fixed and permeabilized as described above. The primary antibodies to detect Golgi, early and late endosome were incubated overnight. The subcellular distribution was analyzed in multiplane z-stack images acquired on confocal microscope Nikon A1R Confocal Microscope (Nikon, New York, USA). Before determining the quantity of colocalization of the green channel (CERT$_L$-GFP) with the magenta channel (GM130, EEA1 or LPBA) by Pearson's correlation coefficient, the images were deconvolved with Nikon NIS-Elements software.

2.10 | Analysis of BODIPY FL C5-Cer redistribution to Golgi and MVE/LE

For BODIPY FL C5-Cer (BODIPY™ FL C5-Ceramide complexed to BSA, ThermoFisher) transport to the Golgi and MVE/LE, HeLa WT or CERT-deficient cells were plated onto bottom glass six wells plates with 14 mm microwells (Cellvis P06-12-0-N). For the Golgi transport, on the day of the experiment cells, were pre-treated with PI4KIIIβ-IN-10 (25 nM and 50 nM) and NC03 (5 and 10 μM) for 15 min. Next, cells were incubated on ice for 20 min with 0.5 μM BODIPY FL C5-Cer in phenol red and serum-free DMEM, and the excess fluorescent dye was removed by washing with serum-free DMEM. Next, BODIPY FL C5-Cer was allowed to be distributed in cells for 10–15 min at 37°C before cells were fixed in 2.5% PFA and 2.5% glutaraldehyde. For the MVE/LE transport, HeLa WT or CERT-deficient cells were transfected with a fusion construct of Rab7a and TagRFP (CellLight™ Late Endosomes-RFP, BacMam 2.0, ThermoFisher) 24 h before incubation with BODIPY FL C5-Cer. The distribution of BODIPY FL C5-Cer was analyzed with the Eclipse Ti2-E inverted confocal microscope using a 100x objective. A minimum of four images with 9–13 planes in Z-direction were acquired for each condition and deconvolved before quantifying Golgi mean fluorescent intensities (MFI) or BODIPY FL C5-Cer correlation to late endosomes-RFP. MFI and correlation were assessed with the Nikon analyzer software.

2.11 | Incubation of cells with fluorescent HPA-12-NBD and bifunctional pacHPA-12

Fluorescent HPA-12 (HPA-12-NBD) was synthesized as previously described (Crivelli et al., 2020). The synthesis of bifunctional HPA-12 (pacHPA-12) is described in Supporting Information. HPA-12-NBD and pacHPA-12 were dissolved in ethanol at 1.77 and 5.5 mM, respectively, and stored at -80°C.

N2a cells were seeded on coverslips or six well glass bottom plates (Cellvis, Mountain View, CA). The following day, cells were transfected with tdTomato-CD9 plasmid for 24–48 h. Then, the medium was changed to a medium containing 1 μM HPA-12-NBD and immediately live-imaged by fluorescent microscopy using a 60× objective.

The bifunctional HPA-12 analogue (pacHPA-12) was used following the protocol previously published for the bifunctional Cer analog (pacFACer) (Jiang et al., 2019). In brief, cells were incubated with 1 μM pacHPA-12 for 15- or 30-min. Cells were washed with medium and then irradiated with UV light (366 nm) for 15 min to cross-link the analogue to CERT. Then, cells were washed with culture medium to remove unbound analogue and three-times with cold DPBS, fixed, and permeabilized as described above. The fluorophore, Alexa Fluor 647 azide was covalently linked to the alkyl group of pacHPA-12 using the

Click-iT™ Cell Reaction Buffer Kit (Thermo Fisher, MA, USA). Next, cells were co-labelled for MVE markers, for example, CD81. Coverslips were mounted and imaged by fluorescence microscopy.

2.12 | EV isolation

2.12.1 | Cell culture supernatant

EVs were isolated from cell culture supernatants by differential ultracentrifugation. N2a cells were grown to 80%–90% confluency and medium replaced with phenol red- and serum-free DMEM medium (Gibco, Invitrogen, CA, USA) and cultivated for 48 h. The media were transferred to a 15 ml Falcon conical tube and centrifuged at $300 \times g$ for 5 min to remove floating cells. Supernatants were collected and centrifuged for 20 min at $4000 \times g$ to remove dead cells and at $10,000 \times g$ for 40 min to collect larger EVs. Lastly, samples were transferred into polypropylene centrifuge tubes (Beckman Coulter, CA, USA), balanced and ultra-centrifuged at $100,000 \times g$ for 2 h. Pelleted EVs were resuspended in 0.1 ml DPBS (Corning, MA, USA). Alternatively, two additional approaches were performed: (1) after the $4000 \times g$ centrifugation step, EVs were isolated with ExoEasy Maxi kit (Qiagen, MD, USA) following the manufacturer's instruction; (2) or after the $100,000 \times g$ centrifugation step, a discontinuous sucrose gradient was used. The gradient formed by 10%, 30%, 40%, and 60% sucrose was spun for 16 h at $100,000 \times g$. The four fractions corresponding to each interface were collected. All fractions were diluted 1:5 in DPBS and centrifuged again for 2 h at $100,000 \times g$. Pellets were dissolved in 0.1 ml of DPBS. The interfaces at 10%–30% and 30%–40% sucrose were positive for the EV marker Alix1.

2.12.2 | Serum

Blood was collected as previously described (Elsherbini et al., 2020). In brief, blood was drawn from the heart and was allowed to clot at room temperature for 30 min. Next, samples were centrifuged at $1800 \times g$ for 10 min at 4°C. to prepare the serum fraction. The clear upper layer (serum) was transferred to a fresh tube and centrifuged at $10,000 \times g$ for 15 min to pellet residual blood cells. Then EVs were isolated from 150 μl of serum using ExoQuick solution (EXOQ; System Biosciences, Inc., Mountain View, CA, USA). The ExoQuick preparation was used for NTA measurement and lipid analysis or further purified with sucrose gradient and NTA measurements repeated.

2.12.3 | Brain tissue

Brains were collected soon after the blood was drawn from the heart. Then, the forebrain was dissected in ice-cold PBS and snap-frozen in liquid nitrogen inside an Eppendorf previously weighed. EVs were isolated as previously described with modifications (Perez-Gonzalez et al., 2017). In brief, frozen forebrain was digested with papain for 20 min at 37°C and passed through a 10 ml serological pipette before the reaction was stopped on ice with proteinase inhibitors. Then, the solution was sequentially centrifuged as follows: $300 \times g$ for 5 min, $4000 \times g$ for 20 min, and $10,000 \times g$ for 40 min. Before precipitating the EVs at $100,000 \times g$, the solution was filtered using a 0.45 μm membrane filter. The precipitate was dissolved in 5% sucrose in DPBS and loaded onto a discontinuous gradient formed by 10%, 30%, 40%, and 60% sucrose in DPBS. The gradient was spun for 16 h with at $100,000 \times g$. Four fractions were collected corresponding to each interface. All fractions were diluted 5-fold in DPBS and centrifuged again for 2 h at $100,000 \times g$. Pellets were dissolved in 0.3 ml DPBS.

Alternatively, after the $10,000 \times g$ centrifugation and 0.45 μm filtration, EVs were collected using the ExoEasy Maxi kit (Qiagen) following the manufacturer's instructions.

2.13 | Nanoparticle tracking analysis (ZetaView) and ExoView

2.13.1 | ZetaView

Nanoparticle Tracking Analysis was performed using a Zetaview instrument. All samples were diluted in DPBS (Corning, MA, USA) before injection into the instrument. Measurement concentrations were determined by pre-testing the ideal particle per frame value (100–200 particles/frame). Optimal camera settings were initially established and kept constant throughout the analyses (Sensitivity: 150–250; Shutter: 74–76; cell temperature: 25°C). After capture, the videos were analyzed by the built-in ZetaView Software. The EV concentration was normalized to the number of cells measured by an automated cell counter (TC20 Biorad), volume of serum, or by tissue weight.

2.13.2 | ExoView

Brain EVs were diluted in Solution A (NanoView bioscience, EV-SOLA10-30) while serum EVs were loaded without purification or dilutions steps. 40 μl of sample were incubated O.N. at RT on pre-scanned ExoView Tetraspanin chips, placed in a sealed 24-well plate. The chips contained spots printed with anti-CD81, or anti-CD9 antibodies or mouse IgG1κ matching isotype antibody, used as a control for non-specific EV binding (NanoView bioscience, EV-TETRA-MI). Chips were then moved to an automated ExoView® CW100 Chip Washer and the tetraspanin program was selected. The following antibody mixture was used to label EVs: anti-Ceramide labelled with anti-rabbit IgG conjugated to Alexa 647 using the Zenon™ Rabbit IgG Labeling Kit (ThermoFisher), anti-CD81 conjugated 555 (NanoView bioscience, EV-mCD81-A-555) and anti-CD9 conjugated 488 (NanoView bioscience, EV-mCD9-A-488), all of them diluted in blocking solution. Chips were then imaged with the ExoView R100 reader using the ExoScan 3.0 acquisition software. Images acquired were analyzed using ExoViewer 3.0 software.

2.14 | Electron microscopy

HeLa WT cell were grown on Costar® 6-well Clear (3506) to 100% confluency, fixed in 4% PFA in PBS for 45 min and permeabilized for 10 min with 50% Ethanol. After washing with PBS, cells were blocked with 3% BSA for 1 h and the anti-CERT antibody (Bethyl Laboratories, A300-669A) was incubated O.N. at 4°C. Next day anti-rabbit IgG Alexa Fluor® 647 Fluoro (1.4nm)Nanogold (Nanoprobes) was incubated for 2 h. Then samples were washed 3× in PBS, post-fixed with 1% glutaraldehyde in PBS (10 min) rinsed with deionized water 2× and HG Silver enhancement kit (Nanoprobes, 2012–45ML) was performed following manufacturer instruction. Samples were rinsed in deionized water and lastly with PBS. Next, samples were incubated with 0.2% osmium tetroxide in PBS (30 min on ice), rinsed with deionized water and exposed to 0.25% Uranyl acetate for 1 h on ice to better preserve immunogold labelling (Tao-Cheng et al., 2021). Finally, samples were dehydrated at room temperature in a graded series of ethanol (4 min interval) at 50%, 70%, 90%, and three changes of 100%, and were embedded after two changes of 100% resin for 45–60 min in 60°C oven. Polymerization was allowed to proceed for 2 days. Embedded cells were separated from the plastic culture ware, trimmed and ~70 nm sections were cut with a microtome and mounted on FCF-200-Cu grids. Brain-derived EVs were fixed in 2% PFA and 5–7 μl were loaded on FCF-200-Cu grids for 1 min and stained with 1% uranyl acetate for 10 s. After excess of uranyl acetate was removed samples were dried before imaging. Images were acquired using a Thermo Scientific™ Talos™ F200X TEM operating at 200 kV accelerating voltage in STEM mode. Low beam current and long dwell times (50 μs) were used to maximize contrast while minimizing beam damage.

2.15 | Cytosolic and membrane-bound protein extraction

Cells were washed with ice-cold DPBS, trypsinized and centrifuged at 300 × g for 5 min at 4°C. The cell pellet was resuspended in 0.5 ml ice-cold homogenization buffer containing 250 mM sucrose, 1 mM EDTA, 10 mM Tris-HCl buffer at pH to 7.2, and Halt™ Protease Inhibitor Cocktail (Thermo Fisher, MA, USA) and sonicated using a probe sonicator. The homogenate was centrifuged at 700 × g for 10 min at 4°C to remove intact cells, nuclei and cell debris. The supernatant was further centrifuged at 100,000 × g for 1 h at 4°C. The supernatant was considered the cytosolic fraction and the pellet was resuspend in 0.5 ml RIPA buffer (250 mM Tris-HCl (pH 7.4), 750 mM NaCl, 5% NP-40, 2.5% sodium deoxycholate, 0.5% SDS) and incubated for 15 min at 4°C with occasional vortexing. Lastly, the sample was centrifuged at 100,000 × g for 30 min at 4°C and the supernatant was transferred to a fresh tube and considered the membrane fraction.

2.16 | Immunoblot analysis

EVs derived from equal amounts of cells, serum or brain were solubilized with 5X Laemmli sample buffer (10% SDS, 250 mM Tris pH 6.8, 1 mg/ml bromophenol blue, 0.5 M DTT, 50% glycerol, 5% β-mercaptoethanol) and heated to 95°C for 5 min. When protein extraction from cells or brain was not prepared by fractionation as explained above protein were extracted in RIPA buffer. Proteins were separated using SDS-PAGE gels (8% or 10%) or pre-cast gels 4%–20% (mini-PROTEAN TGX, Biorad) and transferred to nitrocellulose membranes. After blocking with 5% NFDM (Blotting-grade blocker, Biorad) for 1 h, blots were probed with primary antibodies overnight at 4°C and incubated with an HRP-conjugated secondary antibody. The membranes were developed with Clarity Western ECL Substrate (Biorad) or SuperSignal™ West Femto Substrate (ThermoFisher) and images were acquired on a ChemiDoc imaging system (Biorad).

TABLE 1   List of interactors of CERT$_L$ domains associated to EVs biogenesis

CERT$_L$ domain	Screening	Interactor_Protein name	Gene ID	# Clones	PBS score	Reference
PH domain (N-terminal)	Gal 4	VAMP1	6843	1	D	(Minciacchi et al., 2015)
START domain (C-terminal)	Gal 4	UBAP1	51271	2	C	(Soares Martins et al., 2021)
	LexA	Tsg101	7251	2	D	(Willms et al., 2016)

Note: The number of clones (# clones) represents the number of times the protein emerged during Y2HS screening. For each interaction, a PBS was computed to assess the interaction reliability. This score represents the probability of an interaction to be non-specific, primarily based on the comparison between the number of independent prey fragments found for an interaction and the chance of finding them at random.

2.17 | Sphingolipid analysis

The sphingolipid analyses on cells and cell-derived EVs were performed by the VCU Lipidomics/Metabolomics Core (VLMC). Cell pellets and 100k fractions were analyzed for the following sphingolipids: sphingosine, sphinganine, sphingosine-1-phosphate, sphinganine-1-phosphate, ceramide (N-acyl chain lengths = C14:0, C16:0, C18:1, C18:0, C20:0, C22:0, C24:1, C24:0, C26:1, C26:0), monohexosylceramide (N-acyl chain lengths = C14:0, C16:0, C18:1, C18:0, C20:0, C22:0, C24:1, C24:0, C26:1, C26:0) and SM (N-acyl chain lengths = C14:0, C16:0, C18:1, C18:0, C20:0, C22:0, C24:1, C24:0, C26:1, C26:0).

The sphingolipids of serum and brain-derived EVs were measured by to the lipidomics core facility at the Medical University of South Carolina, Charlston, SC (Dr. Besim Ogretmen, director) (https://hollingscancercenter.musc.edu/) as previously described (Bielawski et al., 2009, 2010).

2.18 | Statistical analysis

The statistical analyses were performed using GraphPad Prism version 8.4.3 (686). Unpaired *t*-test was used for comparing of two means or Whitney Mann test when normality distribution was not met. One-way ANOVA followed by Sidak's or Dunnett's multiple comparisons test was used for comparing more than two conditions or for investigating HPA-12 effect across ceramide or SM species. A *p*-value of <0.05 was considered significant.

3 | RESULTS

3.1 | CERT is associated with MVE and interacts with Tsg101 via the START domain

It has been reported that CERT is important for EV secretion under palmitic acid overload state in hepatocytes (Fukushima et al., 2018). However, it remains unknown whether CERT plays a role in EV formation under physiological conditions and how mechanistically CERT participates in EV biogenesis.

Immunofluorescence labelling in N2a cells showed partial colocalization of CERT with Early Endosome Antigen 1 (EEA1) and lysobisphosphatidic acid (LBPA), which are markers for early and late endosomes/MVE (Figure 1a). A similar pattern was found with primary cultured mouse neurons (Supplementary Figure S1A). CERT also colocalized with other MVE markers such as the cluster of differentiation 9 (CD9) (Supplementary Figure S1B). To analyze whether CERT is released in association with small EVs, we isolated EVs from the culture medium of N2a cells at 90%–100% confluency by using ultracentrifugation on a discontinuous sucrose gradient. The majority of CERT was enriched in the same fraction as the exosomal marker protein Alix (Figure 1b).

Since we found CERT to be part of the MVE and EVs, we tested if CERT interacted with the proteins of the ESCRT complex. Therefore, we screened for possible interactors by using a two-hybrid system with the PH domain, the middle region (comprising the SR and FFAT motifs) and the START domain of CERT, as separate baits. We found that CERT interacted with two proteins (Tsg101 and UBAP1) via the START domain (Table 1). The PH domain interacted with VAMP1, a protein which has been implicated with EV formation (Table 1). Both Tsg101 and UBAP1 are part of the ESCRT-I complex (Minciacchi et al., 2015; Soares Martins et al., 2021). To confirm Tsg101-CERT interaction to be physiologically relevant, we performed a proximity ligation assay (PLA), which yields an in situ fluorescence signal for proteins that are closer than 30–40 nm, suggesting that they form a complex (Jiang et al., 2019). N2a cells were transfected with a tdTomato-CD9 plasmid and then subjected to PLA following incubation with anti-Tsg101 (mouse) and anti-CERT (rabbit) antibodies. Figure 1c shows perinuclear PLA signals, indicating that TSG101 and CERT form a protein complex in tdTomato-CD9 positive intracellular vesicles. These results were corroborated in mouse
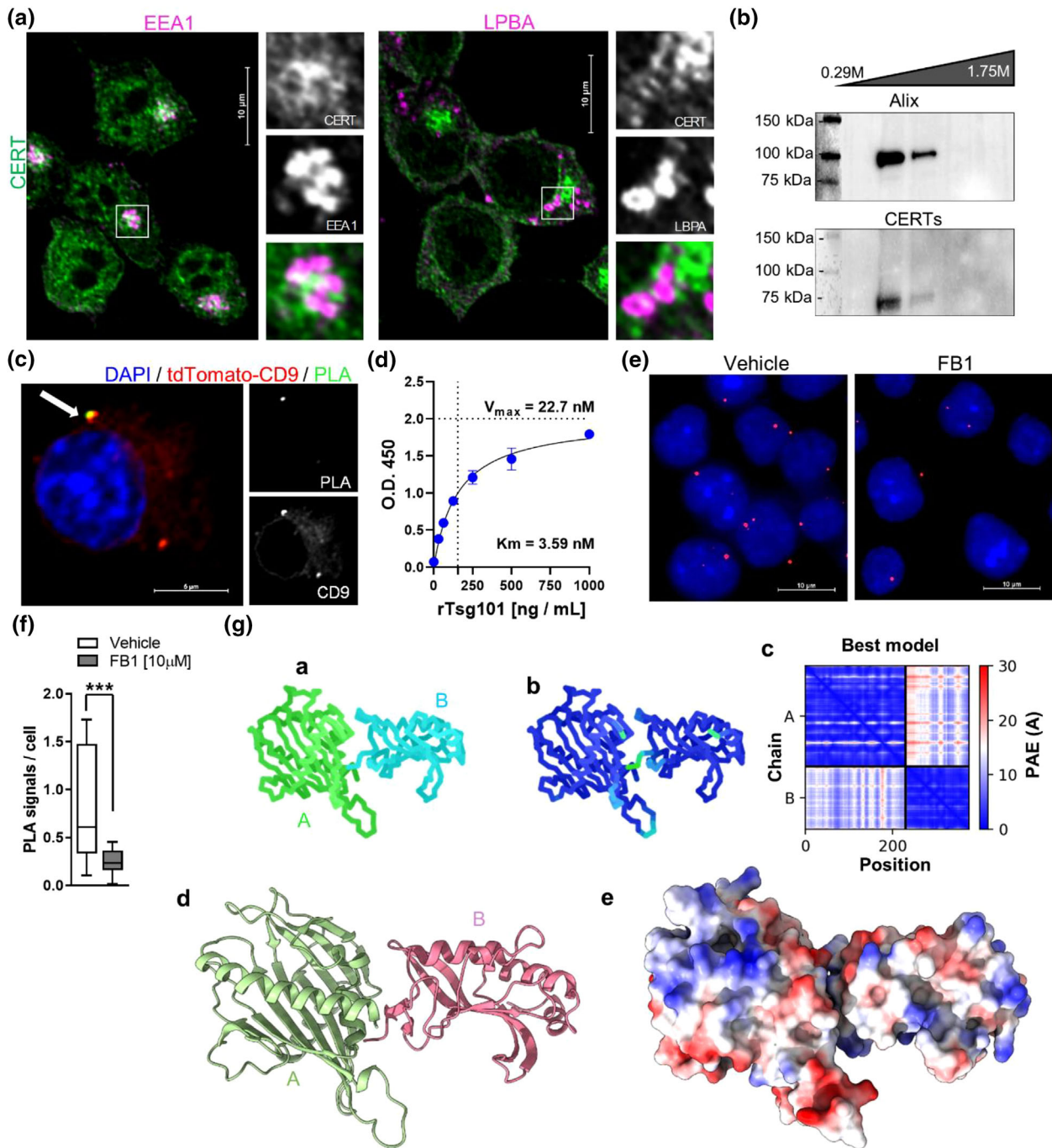
FIGURE 1 CERT is associated with the MVE and interacts with Tsg101. (a) Confocal photomicrograph of fluorescent labelling of CERT (green) showing partial colocalization/juxtaposition (white) with EEA1 or LBPA (magenta) in N2a cells. Scale bar 5 μm. (b) CERT detected by immunoblot in the same fractions of Alix after EV purification by sucrose gradient ultracentrifugation 0.29–1.75M. (c) Confocal photomicrograph of PLA assay (green) in tdTomato-CD9 (red) transfected N2a cells indicating complex formation between Tsg101 and CERT (arrow). DAPI (blue) was used to stain the nuclei. Scale bar 5 μm. (d) Binding kinetics of rTsg101 to immobilized rCERT$_L$ measured by ELISA. The Michaelis-Menten constant (Km) equalled 3.59nM with Vmax equal to 22.7nM. (e) Representative photomicrographs of Tsg101 and CERT PLA signals (red), after treatment with vehicle and 10 μM FB1. Scale bar 5 μm. (f) Box and Whiskers plot of 14–23 pictures per condition, of $n = 3$ independent experiments, showing PLA signals normalized to the number of nuclei (blue). Unpaired t-test (*$p < 0.05$). (g) AlphaFold2 highest-ranked structure prediction of the complex between (a) the human START domain of CERT (green A) and the human UEV domain of Tsg101 (chain coloured in light blue B). In (b) the coloured polymers based on pLDDT (score = 93.3) and in (c) PAE plot (pTMscore = 0.742). In (d) the 3D structure of the complex (START domain in green A and UEV domain in magenta B) and in (e) the colour surface electrostatic potential of the complex.

primary neurons and astrocytes (Supplementary Figure S1C-D). No positive signals were found when performing PLA only with anti-Tsg101 antibody and rabbit IgG as controls. The kinetic of CERT and Tgs101 interaction was established by ELISA using full length human rCERT$_L$ and rTgs101. The rTsg101 concentration at which the reaction rate achieved half of its maximal value (Km) was 3.59 nM (Figure 1d). Also, the reverse set-up with rTsg101 immobilized to ELISA plate and detection with rCERT$_L$ gave positive signals confirming complex formation between Tsg101 and CERT. Of notice, the polyclonal antibody anti-CERT against the first 50 amino acids gave slower kinetics compared to antibody anti-CERT against epitope 300–350 (Supplementary Figure S1E). Since the interaction between Tsg101 and CERT involved the START domain, which binds to ceramide, we determined whether the complex formation was regulated by ceramide. Interestingly, the PLA signals for the Tsg101-CERT complex, were reduced when cells were treated with Fumonisin B1 (FB1), which inhibits ceramide biosynthesis in the ER (Figure 1e-f). Lastly, we modelled the complex using AphaFold2 in CoLabFold which predicted, with high confidence, the structure of the complex between the human START domain of CERT, and the human UEV domain of Tsg101 (Figure 1g).

Of note, even though it was not detected by the two-hybrid system as interaction partner of CERT, immunocytochemistry showed that the tetraspanin like cluster of differentiation 81 (CD81) can be found in close proximity to CERT as indicated by PLA signals. CD81 is a transmembrane protein which takes part in forming the tetraspanin-enriched microdomains (TEM) (Andreu, 2014). TEM have been proposed to play a role in EV biogenesis and sorting of EV cargo (Andreu, 2014; Perez-Hernandez et al., 2013). As for Tsg101 and CERT, the PLA positive signals, between CERT and CD81, were reduced when cells were treated with FB1 (Supplementary Figure S1F-G).

These data indicate that CERT enters the endosomal pathway and is released in EVs. Furthermore, CERT physically interacts with Tsg101 via the START domain and this interaction requires ceramide biosynthesis in the ER.

3.2 | Overexpression of CERT induces EV formation and secretion

The discovery that CERT is found in EVs and forms a protein complex with Tsg101 prompted us to investigate whether CERT is actively taking part in EV biogenesis. To answer this question, N2a were transfected with a control vector expressing GFP or pcDNA 3.1-hCERT expressing human CERT. Overexpression of CERT increased the cytosolic and membrane-bound CERT levels (Supplementary Figure S2A). Consistent with our hypothesis that CERT participates in EV formation, overexpression of CERT increased EV numbers released by N2a cells. NTA measurements showed that both, the 10K and 100k EV fraction isolated by ultracentrifugation were increased significantly by CERT expression after 48 h transfection (Figure 2a). The particle size distribution profile appeared to be different only in the 10K EV fraction, which displayed more than one peak in the particle size distribution upon transfection with the pcDNA3.1-hCERT (Supplementary Figure S2B).

To confirm the NTA results, 100k EVs were subjected to Western blot for quantitation of the EV markers Tsg101, Alix and Flotillin-2, the levels of which were significantly increased after overexpression of CERT (Figure 2b). Furthermore, the concentration of CERT in EVs precipitated at 100k was 3.7× higher with CERT-transfected cells after normalization to Flotillin-2 compared to control vector condition, suggesting that the increment of EV secretion was associated with increase of CERT levels per EV (Figure 2c). In the cytosolic and membrane fractions of cells, no difference was found between the control vector and pcDNA3.1-hCERT in Tsg101, CD81 and N-SMase-2 levels (Supplementary Figure S2C-D).

To explore if the increase of EVs mediated by CERT expression was caused exclusively by the increase of SM levels entering the trans-Golgi network to the plasma membrane, we inhibited N-SMase-2 with the drug GW4869 after transfection with pcDNA3.1-hCERT. We found that GW4869 did not completely reverse the increase of EV secretion mediated by CERT expression (Figure 2d). Additionally, when inhibiting SMS1/2 with D609, the number of EVs increased by about four-fold and CERT was down-regulated in EVs and cells (Figure 2e-f). This suggests that EVs produced by ceramide generated by N-SMase-2 and SMS1/2 are an alternative pathway to CERT-mediated EVs formation.

To determine whether overexpression of CERT was associated with increased complex formation between Tsg101 and CERT, we quantified PLA signals after transfecting N2a cells with control vector or FL-CERT$_L$-GFP. We found that FL-CERT$_L$-GFP transfected cells showed an increased number of positive PLA signals compared to control vector-transfected cells (Figure 2g).

These data indicate that CERT is participating in EV biogenesis by interaction with the ESCRT-dependent pathway machinery and not only by providing the substrate SM to N-SMase-2 and/or ceramide to SMS2.

3.3 | The PH domain is necessary for CERT to enter the endocytic pathway and for redistribution of ceramide to MVE

The trans-Golgi network and the early endosome create a hub where protein cargo and sphingolipid profile of EVs are likely determined. Therefore, we tested if sorting of CERT to the MVE requires the protein to anchor the trans-Golgi via the PH domain, a protein domain binding to PI4P (Sugiki et al., 2012). We generated a plasmid containing cDNA encoding PH-deficient CERT$_L$ tagged to GFP as described in Section 2. After transfecting N2a cells with PH-deficient-CERT$_L$-GFP or full length
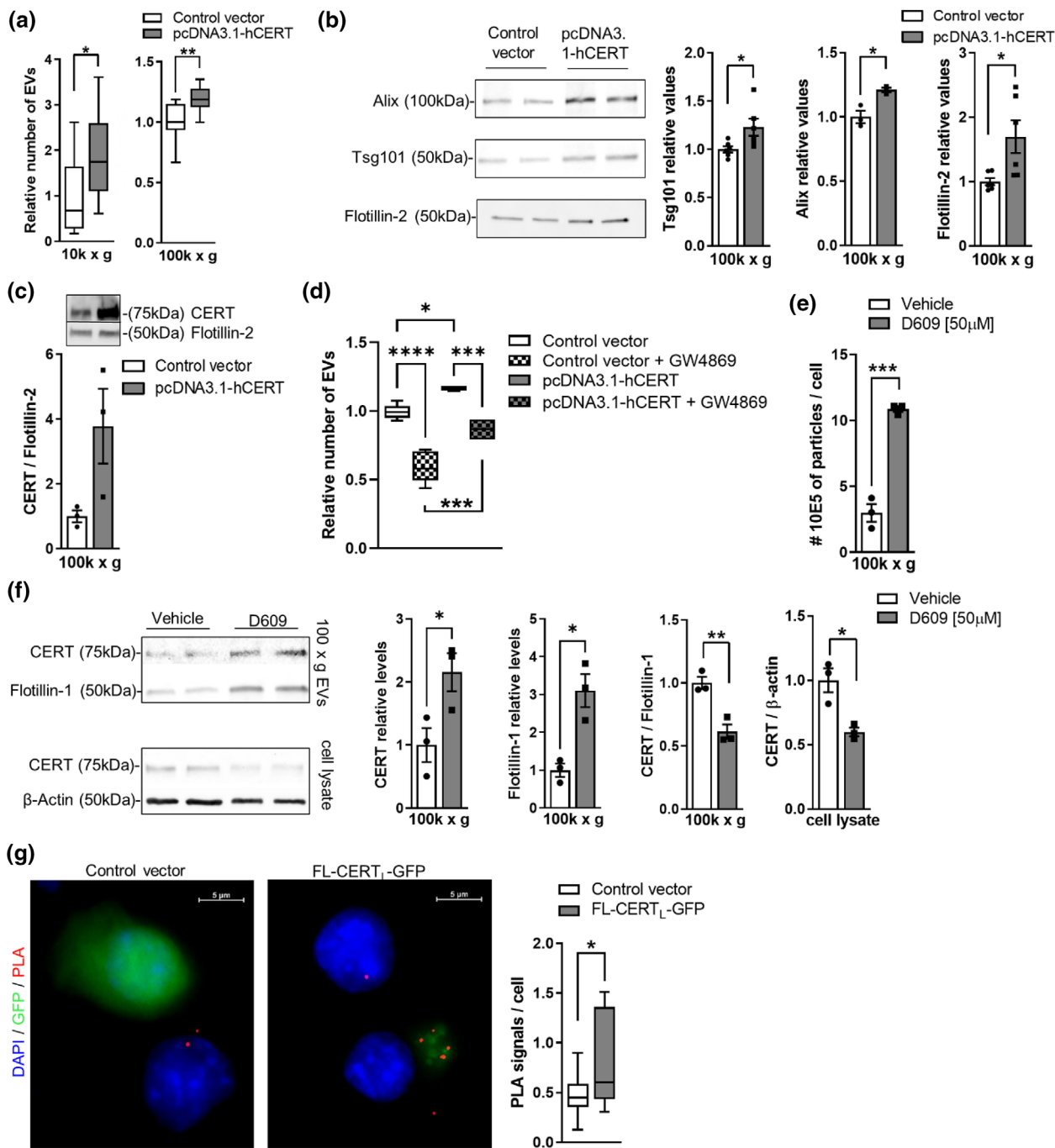
FIGURE 2 Overexpression of CERT induces EV formation and secretion. (a) Numbers of EVs in the 10K and 100k EV fractions measured by NTA after pcDNA-hCERT transfection. Box and Whiskers plot represent $N = 6$/group. (b) Quantification of Tsg101, Alix and Flotillin-2 by Western blots. Bar graphs represent average ± SEM of $N = 6$/group. (c) Enrichment of CERT in 100k EV fraction after transfection with pcDNA-hCERT. Intensities of bands corresponding to CERT were normalized to Flotillin-2. Bar graph represents average ± SEM with $N = 3$/group. (d) The 100k EVs numbers measured by NTA after pcDNA-hCERT transfection and co-treatment of the N-SMase2 inhibitor GW4869 (15 μM). Box and Whiskers plot represents $N = 4$–9/group. One-way ANOVA, Sidak's posthoc testing (*$p < 0.05$; ***$p < 0.001$; ****$p < 0.0001$). (e) The 100k EV numbers measured by NTA after treatment with D609 (50 μM). Bar graph represents average ± SEM with each $N = 3$/group. (f) Quantification of CERT by immunoblots after treatment with D609 (50 μM) in EVs and cell lysate. Bar graphs represent average ± SEM with each $N = 3$/group. (g) Representative photomicrographs of Tsg101 and CERT PLA signals (red), after transfection with control vector (green) or FL-CERT$_L$-GFP (green). Scale bar 5 μm. Box and Whiskers plot of three independent experiments including a total of 16 pictures/condition showing PLA signals normalized to the number of nuclei (blue). Unpaired t-test (*$p < 0.05$).

(FL)-CERT$_L$-GFP, the distribution of the GFP-tagged protein was tracked by confocal microscopy. Cells grown on coverslips were immunolabeled to quantify the levels of CERT$_L$ specifically in the Golgi region (anti-GM130), early endosome (EEA-1) and late endosomes (anti-LBPA). As expected, the FL-CERT$_L$-GFP protein strongly colocalized with the Golgi, while the PH-deficient-CERT$_L$-GFP protein was more diffused in the cytosol (Figure 3a). Quantification of the green fluorescent intensity emitted by CERT$_L$-GFP in the Golgi co-immunolabeled with GM130 was significantly higher compared to PH-deficient-CERT$_L$-GFP (Figure 3b). The removal of the PH domain also significantly reduced the association of early and late endosome immunolabeling with CERT$_L$-GFP fluorescence (Figure 3c-f). Furthermore, the CERT-deficient HeLa cell line which expresses a truncated form of CERT, missing the PH domain, displayed a reduced number of small EVs compared to the HeLa WT cell line (Supplementary Figure S3A-C), absent BODIPY FL C5-Cer distribution to the Golgi region and diminished redistribution of BODIPY FL C5-Cer to the MVE labelled by Rab7a and TagRFP (Figure 3g-h).

This data indicates that the PH domain is critical for CERT to enter the endocytic pathway and for ceramide to be translocated to the MVE.

3.4 | PI4P produced by PI4KIIα controls CERT-mediated ceramide transport from the ER to the MVE and CERT-mediated EV formation

It has been reported that the ER forms contact sites with the MVE (Raiborg et al., 2015). Furthermore, a direct lipid transport between the ER and MVE has been described at membrane contact sites (Wilhelm et al., 2017). Since we found that CERT-deficiency reduces ceramide translocation to the MVE we explored if this was a consequence of a reduction of ceramide transfer to the Golgi apparatus or by a reduction of ceramide transfer (CERT-mediated) between ER and endosomes.

The ceramide transport to the Golgi apparatus is regulated by the interaction of the PH domain of CERT with PI4P generated by PI4IIIβ kinases (De Matteis et al., 2013; Sugiki et al., 2012). Pharmacological inhibition of PI4 kinases reduces SM generation, which is dependent on CERT function (Kumagai & Hanada, 2019; Sugiki et al., 2012). This reduction is most likely due to the depletion of PI4P, which decreases CERT engagement to the *trans*-Golgi and limits SM production. Firstly, with HeLa WT cells we tested if the highly specific PI4KIIIβ inhibitor, PI4KIIIβ-IN-10 (Rutaganira et al., 2016), reduced CERT-dependent ceramide transport from the ER to Golgi by tracking BODIPY FL C5-Cer. HeLa cells were used for better visibility of BODIPY FL C5-Cer transport and for comparison to CERT-deficient cells which completely lack this transport. As expected, the PI4KIIIβ inhibitor reduced BODIPY FL C5-Cer redistribution to the Golgi (Supplementary Figure S3D-E). Meanwhile, we hypothesized that CERT-mediated transport of ceramide between the ER and MVE, was controlled by the interaction between the PH domain of CERT and PI4P generated by PI4KIIα at endosomes. In HeLa WT cells we found CERT to be located in the proximity of the ER-MVE contact sites by confocal microscopy and TEM (Figure 4a-c). Additional TEM images localizing CERT at the limiting membrane of MVE are reported in Supplementary Figure S3F. Next, to test that CERT transports ceramide from the ER and to the MVE, we specifically inhibited PI4KIIα with the drug NC03 (Sengupta et al., 2019). To employ a dose of NC03 that was not affecting the PI4P levels in the Golgi, we traced BODIPY FL C5-Cer redistribution and tested different concentrations of NC03 in HeLa WT cells. We found that 5 μM (or lower concentration) of NC03 did not affect BODIPY FL C5-Cer redistribution to the Golgi (Figure 4d and e).

Next, in N2a cells, we investigated the effect of the PI4KIIIβ and PI4KIIα inhibitors on EV biogenesis. The number of EVs was reduced in cells treated with PI4KIIIβ and PI4KIIα inhibitors (Figure 4f-g), while the levels of the EV marker Flotillin-1 remained unchanged in cell lysate (Supplementary Figure S3G). It is important to highlight that PI4KIIIβ-IN-10 and NC03 had no effect on the EV number in CERT-deficient HeLa cells, confirming that PI4KIIIβ and PI4KIIα inhibitors mode of action are dependent on CERT function (Supplementary Figure S3H). Furthermore, by mass spectrometry, we found that only the PI4KIIα inhibitor reduced the C16:0 ceramide content in EVs (Figure 4h).

This data indicates that there are two pathways for CERT mediated EV biogenesis: one which is determined by CERT engaging the Golgi apparatus which is regulated by PI4KIIIβ and a second which is controlled by the interaction of the PH domain of CERT with PI4P produced by PI4KIIα in endosomes. Furthermore, the PI4KIIα dependent pathway determines the ceramide content in EVs.

3.5 | CERT inhibitor HPA-12 reduces formation and sphingolipid content of EVs

We used HPA-12, a CERT inhibitor first described by Hanada (Yasuda et al., 2001), to further study the effect of CERT on EV biogenesis. HPA-12 has to be in (1*R*,3*S*) configuration to successfully block ceramide from the START domain of CERT (Berkeš et al., 2016). Racemic preparation or other configurations like (1*R*,3*R*)-diastereoisomer are 4–20 times less potent in cell-free competition assays for the START domain (Santos et al., 2015).

Firstly, to study cell uptake and distribution of HPA-12, we designed and synthesized the fluorescent and photoactivatable analogues of HPA-12, NBD-HPA-12 and pacHPA-12. Incubation of N2a cells with fluorescent HPA-12 (NDB-HPA-12) showed
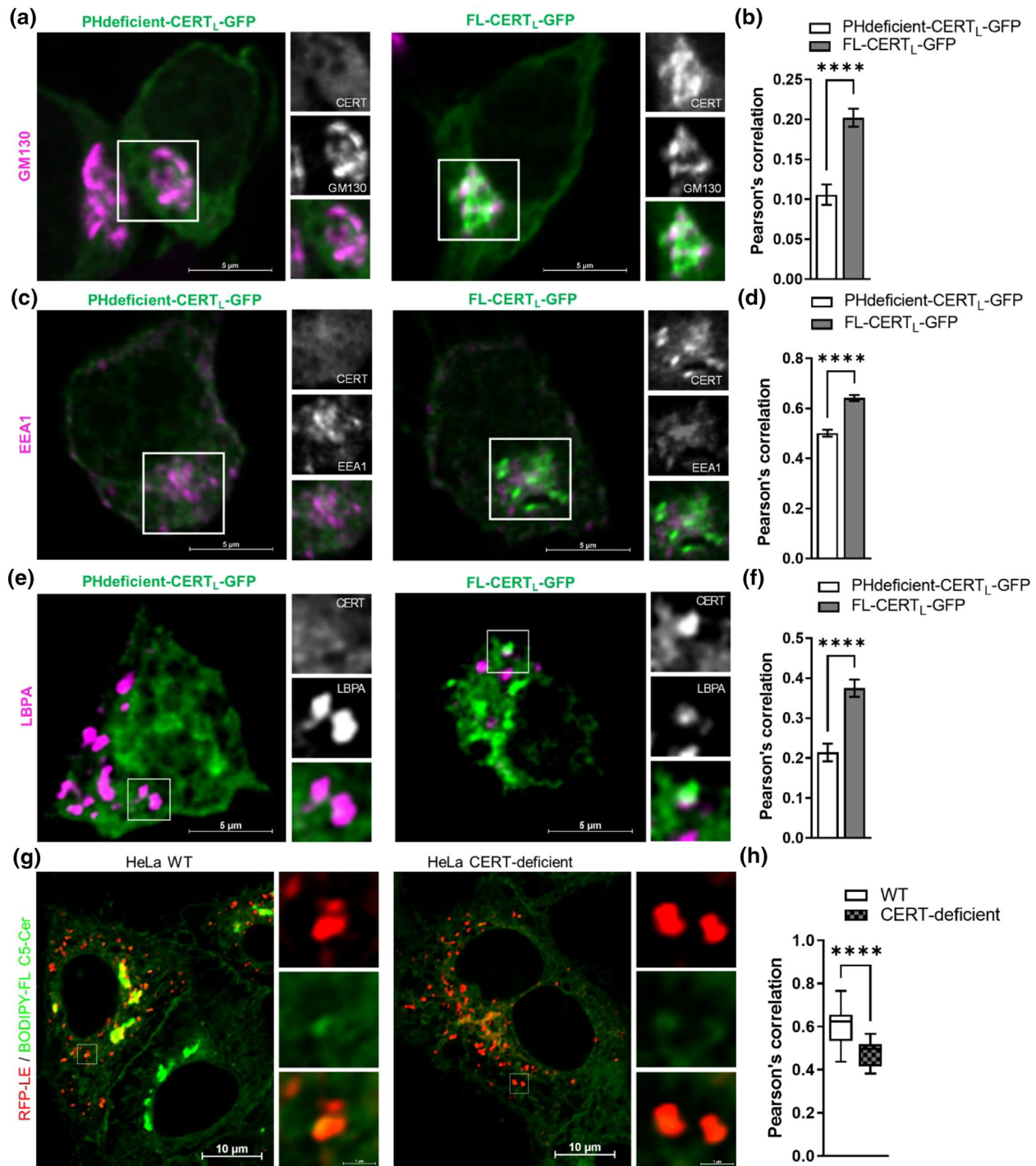
FIGURE 3 The Interaction of PI4P with the PH domain is necessary for CERT to enter the endocytic pathway and for redistribution of ceramide to the MVE. (a) Confocal photomicrographs displaying partial colocalization between PHdeficient-CERT$_L$-GFP or FL-CERT$_L$-GFP and the Golgi, immunolabeled with anti-GM130. Scale bar 5 μm. (b) Correlation coefficient of fluorescence intensities of PHdeficient-CERT$_L$-GFP or CERT$_L$-GFP and GM130 (Golgi apparatus) immunolabeling. Bar graph represents $\pm$ SEM of nine photomicrographs per condition. Unpaired t-test was applied, ***$p < 0.001$. (c) Confocal photomicrographs displaying colocalization between PHdeficient-CERT$_L$-GFP or CERT$_L$-GFP and early endosome, immunolabeled with anti-EEA1 antibody. Scale bar 5 μm. (d) Correlation coefficient of fluorescence intensities of PHdeficient-CERT$_L$-GFP or CERT$_L$-GFP and EEA1 immunolabeling. Bar graph represents average $\pm$ SEM of nine photomicrographs per condition. Unpaired t-test was applied, **$p < 0.01$. (e) Confocal photomicrographs displaying colocalization between PHdeficient-CERT$_L$-GFP or CERT$_L$-GFP and late endosomes, immunolabeled with anti-LBPA antibody. Scale bar 5 μm. (f) Correlation coefficient of fluorescence intensities of PHdeficient-CERT$_L$-GFP or CERT$_L$-GFP and LPBA immunolabeling. Bar graph represents mean $\pm$ SEM of nine photomicrographs per condition. Unpaired t-test was applied, ***$p < 0.001$. (g) Confocal photomicrographs showing BODIPY FL C5-Cer redistribution to the LE/MVE In HeLa-WT and HeLa CERT deficient cell line. (h) Pearson's correlation of fluorescence intensities of BODIPY FL C5-Cer and RFP-LE Whiskers plot represent average $\pm$ SEM of $N =$ photomicrographs/group. Unpaired t-test was applied, ****$p < 0.001$.
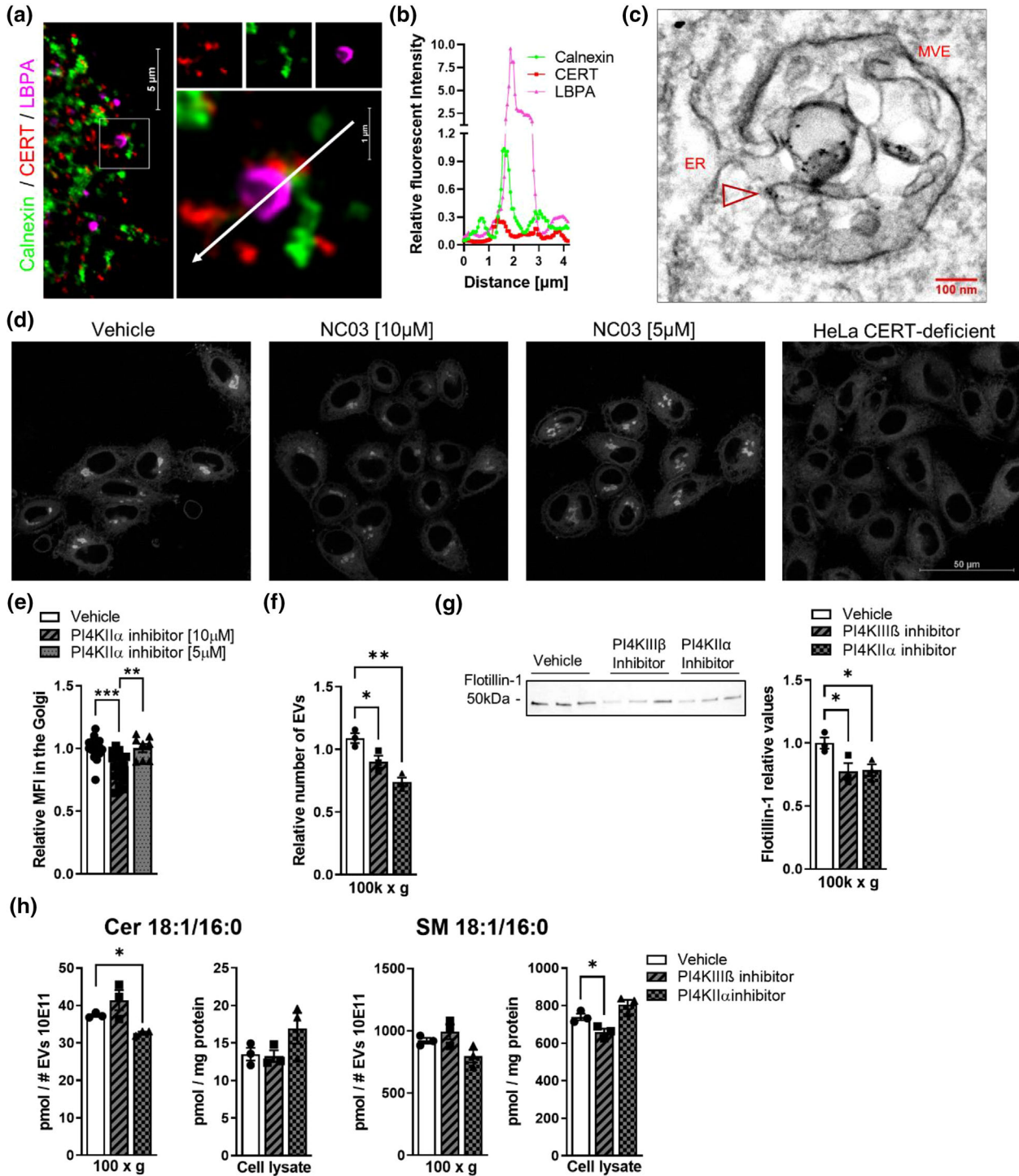
FIGURE 4 PI4P produced by PI4KIIα controls a direct ceramide transport from the ER to the MVE and CERT-mediated EV generation. (a) Confocal photomicrographs displaying immunolabeled CERT (red) partially colocalizing with the ER immunolabeled with Calnexin (green) and MVE immunolabeled with LBPA (magenta) at contact sites. (b) Linescan analyses with fluorescence intensities of the ER (Calnexin), MVE (LPBA) and CERT along the arrow shown in A. (c) TEM image of Immunogold labelling of CERT in the limiting membrane of MVE and in proximity to ER. Arrow shows labelling on limiting membrane of MVE. (d) Confocal photomicrographs showing BODIPY FL C5-Cer redistribution to the Golgi region without or with PI4KIIα inhibitor (NC03) 10 μM or 5 μM. HeLa CERT-deficient cell line was used as negative control. (e) Quantification of the relative MFI measured at the Golgi region after BODIPY FL C5-Cer incubation in absence or presence of 10 μM or 5 μM of PI4KIIα inhibitor. Bar graph represents average ± SEM of N = 8–18/group. One-way ANOVA, Tukey's posthoc testing (*p < 0.05; **p < 0.01). (f) Number of EVs in the 100k fraction measured by NTA after 24 h incubation with vehicle, 50 nM of PI4KIIIβ inhibitor or with 5 μM of PI4KIIα inhibitor (NC03). Bar graph represents average ± SEM of N = 3/group. One-way ANOVA, Sidak's posthoc testing (*p < 0.05; **p < 0.01). (g) Quantification of Flotillin-1 by Western blots. Bar graphs represent average ± SEM of N = 3/group. (h) Cer d18:1/16:0 and SM d18:1/16:0 levels measured in the 100k × g EV fraction or cell lysate after 24 h incubation with vehicle, 50 nM of PI4KIIIβ inhibitor or with 5 μM of PI4KIIα inhibitor (NC03). Bar graph shows average ± SEM with N = 3/group. One-way ANOVA, Sidak's posthoc testing (*p < 0.05).
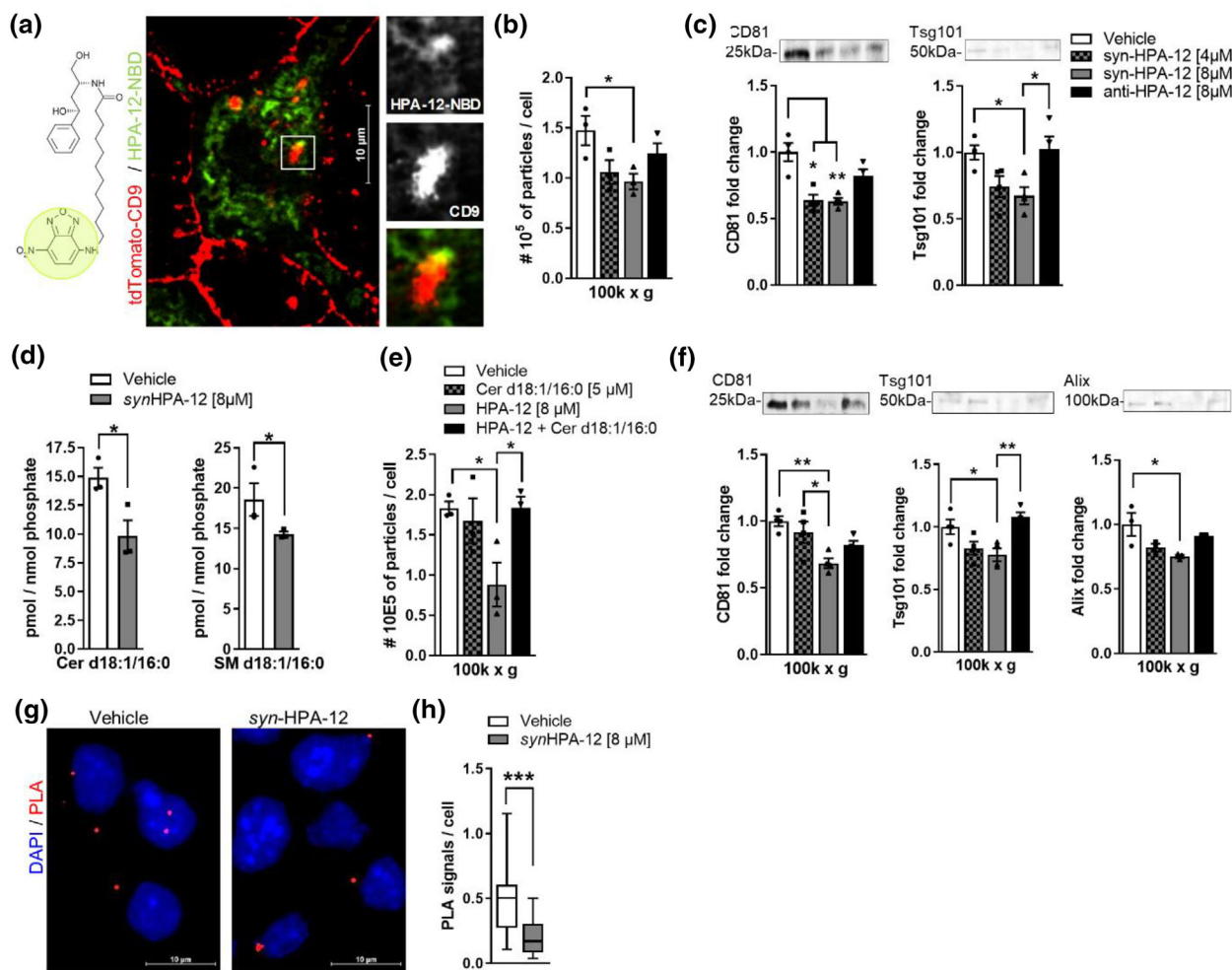
FIGURE 5 CERT inhibitor HPA-12 reduces production and sphingolipid content of EVs. (a) Fluorescent HPA-12 (HPA-12-NBD) chemical structure. Single plane photomicrograph of fluorescence live microscopy of HPA-12-NBD-treated (green) and tdTomato-CD9 (red) transfected cells showing partial colocalization. Scale bar 10 μm. b) 100k EV numbers measured by NTA and normalized to cells after 24 h treatment with *syn*-HPA-12 or the less potent stereoisomer *anti*-HPA-12. Bar graph shows average $\pm$ SEM of $N = 3$/group. One-way ANOVA, Tukey posthoc testing (*$p < 0.05$). (c) Quantification of CD81 and Tsg101 by Western blots. Bar graphs show average $\pm$ SEM of $N = 4$/group. One-way ANOVA, Tukey posthoc testing *$p < 0.05$. (d) Cer d18:1/16:0 and SM d18:1/16:0 levels measured in the 100k EVs fraction. Bar graphs show average $\pm$ SEM with $N = 3$/group. Unpaired *t*-test (*$p < 0.05$). (e) 100k EVs numbers measured by NTA and normalized to cells after 24 h treatment with *syn*-HPA-12 and/or Cer d18:1/16:0. Bar graph shows average $\pm$ SEM with $N = 3$/group. One-way ANOVA, Tukey's posthoc testing (*$p < 0.05$). (f) Quantification of CD81, Tsg101 and Alix by Western blots. Bar graphs show average $\pm$ SEM of two independent experiments with each $N = 4$/group. One-way ANOVA, Tukey's posthoc testing *$p < 0.05$. (g) Representative photomicrographs of Tsg101 and CERT PLA signals after treatment with vehicle or synHPA-12 (8 μM). Scale bar 10 μm. (h). Box and Whiskers plot of PLA signals normalized to the number of nuclei of three independent experiments including a total of 12–20 pictures/condition. Unpaired *t*-test (***$p < 0.001$).

instantaneous cell uptake and colocalization with transiently expressed tdTomato-CD9 (Figure 5a). A fluorescent signal was detected in the 10K and 100k EV fractions after 24 h incubation with NDB-HPA-12 (Supplementary Figure S4A). When using the bio-orthogonal form of HPA-12 (pacHPA-12), we detected intracellular colocalization between pacHPA-12 conjugated to Alexa Fluor 647 azide by click chemistry and immunolabeled CD81 (Supplementary Figure S4B). Taken together this data implies that is HPA-12 is found in proximity of the MVE and is released in association with EVs.

The IC50 of HPA-12 was previously established in a cell-free assay to be 4 μM (Santos et al., 2015). Incubation for 48 h with HPA-12 reduced 100k EVs release dose-dependently, and only in the most active stereochemical configuration, *syn*-HPA-12 (Figure 5b). To confirm a reduction of EV secretion, we performed Western blots for CD81 and Tsg101 in the 100k EV fractions (Figure 5c). No differences in Tsg101 were found in the cell lysate (Supplementary Figure 4C).

It has been reported that HPA-12 reduces SM synthesis by interfering with the CERT-mediated ceramide transfer from the ER to the *trans*-Golgi (Yasuda et al., 2001). However, the effects on ER-to-MVE transfer and ceramide and SM content in EVs are not known. Cell pellets and the 100k EV fractions were analyzed for sphingolipids. In the 100k EV fraction, the content of ceramide, SM, sphingosine and sphinganine were significantly reduced (Supplementary Figure S4D). In particular, ceramide d18:0/16:0 and SM d18:0/16:0 levels were reduced by incubation with *syn*-HPA-12 (Figure 5d). Our data indicated that HPA-12 had

no significant impact on monohexosylceramides, ceramide and SM determined in the cell pellet (Supplementary Figure S4E). In addition, sphingosine and sphinganine, as well as their phosphorylated forms were unchanged (Supplementary Figure S4E). When N2a cells were co-incubated with exogenous ceramide d18:0/16:0 and HPA-12, EV numbers were restored (Figure 5e). This was confirmed by Western blot for CD81, Tsg101 and Alix (Figure 5f).

We also tested if HPA-12 interfered with the interaction between CERT and Tsg101 by treating cells with or without HPA-12 for 24 h. The number of positive PLA signals per cell was significantly reduced in the HPA-12 treated cells (Figure 5g-h).

This data suggests that HPA-12 interference with ceramide transport reduces the formation and sphingolipid content of EVs. Furthermore, HPA-12 interferes with CERT-Tsg101 complex formation probably by displacing ceramide from the START domain.

3.6 | HPA-12 decreases total ceramides levels in blood circulating EVs and total SM levels in brain-derived EVs

Previously, we have determined that HPA-12 crosses the blood-brain barrier and reaches the brain parenchyma intact, suggesting that it is bioavailable for CERT in the brain (Crivelli et al., 2017). To investigate if HPA-12 could reduce numbers and ceramide content in brain EVs, we administered the drug for 1 week every other day at a dose of 2 μg/g body weight (Figure 6a).

The drug had no effect on the body weight (Supplementary Figure S5A). After 7 days of treatment with vehicle or HPA-12, NTA analysis of EVs isolated from serum, using the ExoQuick precipitation method, showed no difference in EV numbers between groups (Figure 6b). When further purifying the ExoQuick samples through a sucrose gradient the number of EVs were similar in vehicle and HPA-12 groups (Supplementary Figure S5B). However, the ceramide content, as measured in the ExoQuick preparation, was reduced in the HPA-12-treated group (Figure 6c). These findings were confirmed by ExoView where serum-derived CD81+ and CD9+ EVs were counted (Figure 6d). In addition, the levels of ceramide positive EVs in CD81+ particles were significantly reduced (Figure 6e).

The EVs were isolated from the brain by discontinuous sucrose gradient or the ExoEasy kit as explained in the Method section. The number of EVs was determined in the fractions enriched with CD81 (interface 10%–30% and 30%–40%). The homogeneity/purity of the EV preparation was confirmed by Western blot and TEM (Supplementary Figure S5C and D). The numbers of EVs, normalized by tissue weight, were similar in the HPA-12 treated group compared to the vehicle group (Figure 6f). A similar result was obtained with the ExoEasy purification method after enumeration by NTA and ExoView (Supplementary Figure S5E and S5F). While the content of SMs was reduced in the HPA-12 treated group, the ceramide levels were similar (Figure 6g-h). This data suggests that in vivo, CERT inhibition with HPA-12 may not affect the total number of EVs, but it changes the EV sphingolipid composition by reducing ceramide and SM.

4 | DISCUSSION

In this study, we provide several lines of evidence that CERT plays a role in the biogenesis and regulation of the sphingolipid composition of EVs. CERT enters the endocytic pathway and is released in association with EVs. Furthermore, CERT transfers ceramide from the ER to the endosome at contact sites. This ceramide transport is regulated by the interaction of the PH domain of CERT with PI4P produced by PI4KIIα in endosomes. Furthermore, a complex is formed between the START domain of CERT, which binds to ceramide, and Tsg101, which is part of the ESCRT-I complex. Inhibition of ceramide biosynthesis in the ER reduces the number of CERT-Tsg101 complexes per cell, while overexpression of CERT increases the number of CERT-Tsg101 complexes and number of EVs. Consistently, functional inhibition of CERT with HPA-12 reduces CERT-Tsg101 complexes, EV numbers and sphingolipid content of EVs. Altogether our data suggest two routes by which CERT regulates EVs: the indirect pathway via the *trans*-Golgi network and the direct pathway via ER-endosomes contact sites.

The *trans*-Golgi network and the early endosome create a hub where the protein cargo and sphingolipid profile of EVs are likely determined (Nagano et al., 2019). We show that CERT partially colocalizes with the early and late endosomes. This finding agrees with the observation made by Fukushima et al., on hepatocytes showing that CERT was distributed to the MVE (Fukushima et al., 2018). Our data show that the recruitment of CERT to the endosomal pathway and MVE is dependent on PI4P production. The PH domain of CERT has a high affinity for PI4P-embedded in phospholipid membranes, which are typical domains of the Golgi membranes (De Matteis & D'angelo, 2007; Sugiki et al., 2012). The pool of PI4P required for CERT to anchor to the *trans*-Golgi region is primarily generated by PI4KIIIβ (Kumagai & Hanada, 2019). Removal of the PH domain of CERT reduced the distribution of CERT to the Golgi apparatus, and early and late endosomes. Additionally, inhibition of PI4KIIIβ reduced EV release. This suggests that the generation of PI4P and its interaction with the CERT PH domain is necessary for CERT association and biogenesis of EVs. Figure 7 shows that this indirect pathway of CERT for EV formation is probably associated with SM production at the *trans*-Golgi and the activity of other enzymes such as N-SMase-2, SMS1 and SMS2, which are known
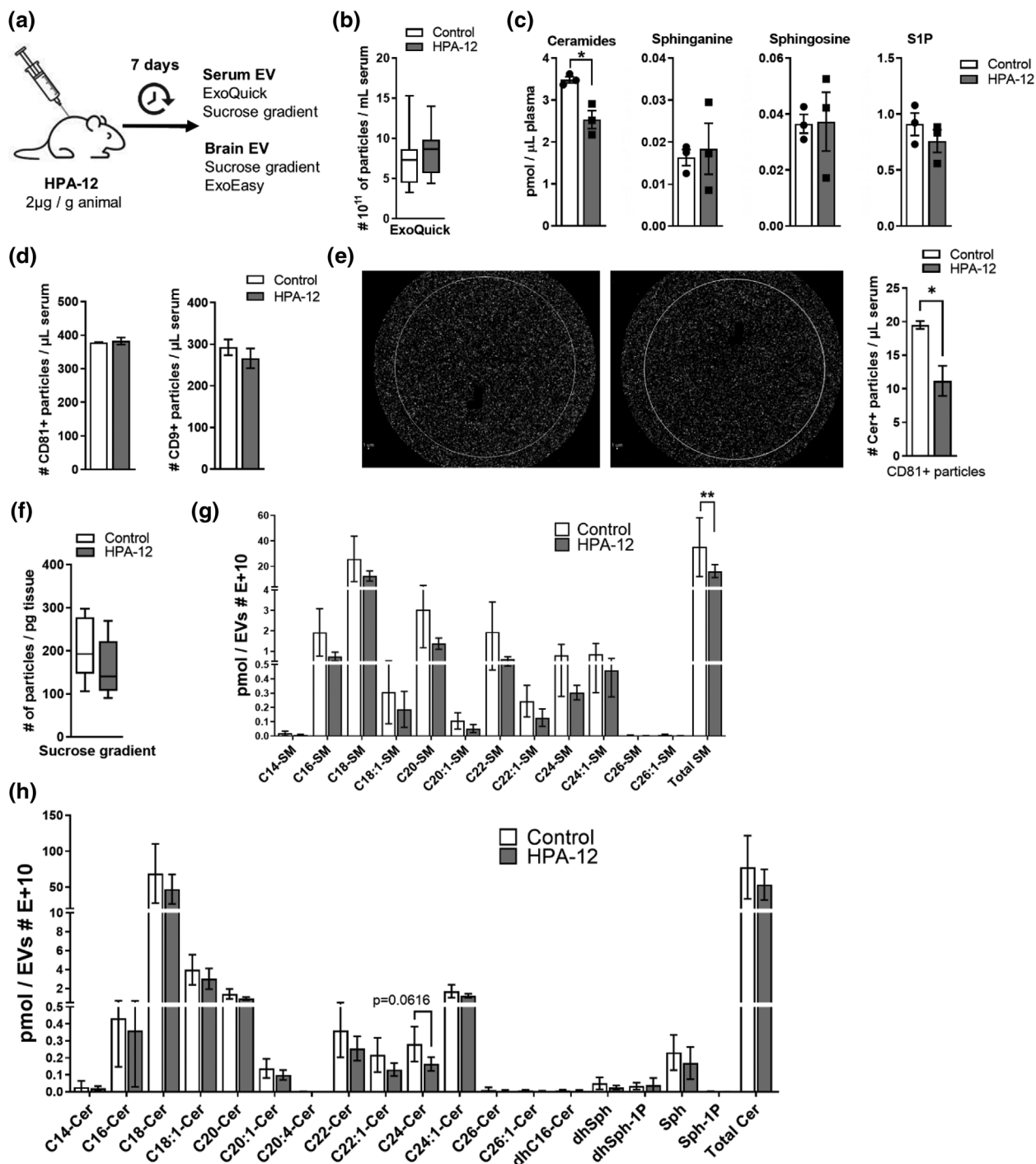
FIGURE 6 HPA-12 decreases ceramide levels in blood circulating EVs and total SM in brain EVs. (a) Animals were treated with HPA-12 for 7 days. Dose was given intraperitoneally every other day. EVs were isolated from serum and brain. (b) NTA measurement of EVs isolated from serum with ExoQuick. Box and Whiskers plot represents the distribution of 10 animals per condition. (c) Quantification of ceramide, S1P, sphingosine and sphinganine by mass spectrometry in EVs isolated from serum with ExoQuick. Bar graphs represent average ± SEM with each $N = 3$/group. Unpaired t-test (*$p < 0.05$). (d) Representative particle counts on different CD81 and CD9 capture spots. Bar graphs represent average ± SEM. for three capture spots of $N = 4$ (pooled)/group of two chips. (e) Representative images for ceramide detection in CD81+ EVs. Representative particle counts on different of ceramide + EVs. Bar graph represents average ± SEM. for three capture spots of $N = 4$ (pooled)/group of two chips. (f) NTA measurement of EVs isolated from brain with sucrose gradient in fractions enriched with Alix1. Box and Whiskers plot represent the distribution of 10 animals per condition. (g) Quantification of SMs C14:0, C16:0, C18:0, C18:1, C20, C20:1, C22:0, C24:0, C24:1, C26:0, and C26:1 by mass spectrometry of brain EVs. Bar graph represents average ± SEM with each $N = 3$–5/group. One-way ANOVA followed by Sidak's multiple comparison (**$p < 0.01$). (h) Quantification of ceramide, S1P, sphingosine and sphinganine by mass spectrometry of brain EVs. Bar graph represents average ± SEM with each $N = 4$-5/group. Unpaired t-test ($p = 0.061$).
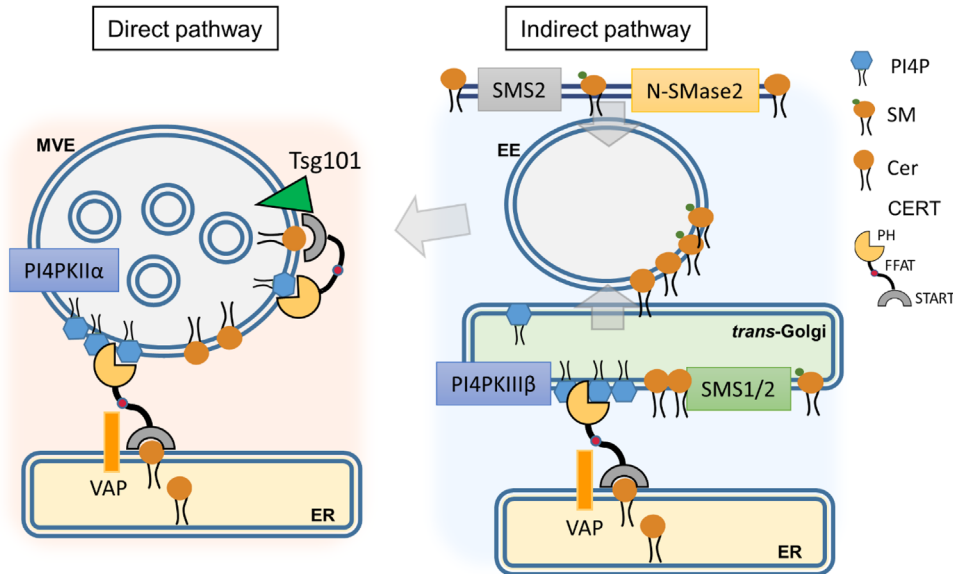
FIGURE 7 Schematic representation of CERT function in EV biogenesis. There are two routes for CERT-mediated EV biogenesis. The indirect pathway via the *trans*-Golgi network which is regulated by PI4P generated by PI4PIIIβ and involves SM production. This pathway is related to SMS1, SMS2 and N-Smase-2 dependent EV formation. The direct pathway is located in ER-endosomes/MVE contact sites. The enzyme PI4PIIα regulates CERT transfer of ceramide to the MVE. At the MVE, a complex is formed by Tsg101 and CERT, which requires ceramide.

to regulate EV biogenesis (Trajkovic et al., 2008). In fact, inhibition of the PI4P pool in the Golgi also reduces transfer of ceramide to the Golgi and SM production.

In contrast to the indirect pathway, the direct pathway of CERT for EV formation does not require SM production or other enzymes of the sphingolipid pathway (Figure 7). In fact, we discovered a direct ceramide transport mediated by CERT at ER-endosomes contact sites. The regulation of this transport is likely dependent on the interaction of the PH domain of CERT with PI4P produced by PI4KIIα in endosomes. During remodelling of early endosomes to late endosomes, PI4P levels increase significantly in late endosomes (Yoshida et al., 2017), providing CERT an anchor to transport ceramide from the ER to late endosomes. The PI4P formed in endosomes is generated mainly by PI4KIIα and not PI4KIIIβ (Henmi et al., 2016). In fact, specific inhibition of PI4P generation in endosomes reduced redistribution of ceramide in EVs and the number of EVs released. However, we cannot completely exclude that there might be other binding partners through which CERT engages the endosomes and that there might be other regulators in addition to PI4KIIα which controls CERT recruitment to the endosomes. Our data suggest a new role of ceramide in EV biogenesis. We show that ceramide biosynthesis regulates the formation of the complex between Tsg101 and the START domain of CERT. Thus, the inhibition of ceramide biosynthesis reduced CERT-Tsg101 complexes. This was further confirmed using HPA-12 which interfered with CERT-Tsg101 complex formation by probably displacing endogenous ceramide from the START domain. Upon CERT overexpression, the number of EVs and CERT-Tsg101 complexes increased. This ceramide-dependent pathway did not seem to be dependent on N-SMase-2 or SMS2. Therefore, the increase of EV production, upon CERT overexpression, may be triggered by enrichment of ceramide in EVs or by ceramide acting as a "switch-on" inducing complex formation between CERT and Tsg101.

How sphingolipids are enriched in EVs is not completely understood. However, ceramide levels in EVs are highly important in disease condition (Elsherbini & Bieberich, 2018). Recently, Dichlberger et al., found that the ceramide interacting protein, lysosome-associated protein transmembrane 4B (LAPTM4B), regulates the glycosphingolipid composition of small EVs (Dichlberger et al., 2021). Interestingly, LAPTM4B deficiency increased glycosphingolipids in the EVs, leaving ceramide unaffected even though LAPTM4B regulates the subcellular distribution of ceramide (Dichlberger et al., 2021). In our study, when the ceramide transporter function of CERT was inhibited with HPA-12, not only EVs were decreased in numbers, but also in their content of ceramide, SM, sphingosine and sphinganine, while glycosphingolipids were poorly affected. In particular, Cer d18:0/16:0 and SM d18:0/16:0 levels were reduced by HPA-12 treatment: This result agrees with the observation of Fukushima et al, showing that CERT mediated enrichment of EVs with Cer d18:1/16:0 under lipotoxic stress in hepatocytes. Consistently, down-regulation of CERT reduced the Cer d18:1/16:0 content in EVs (Fukushima et al., 2018). In other studies, Cer d18:1/16:0 overload in neurons or in muscle, under disease conditions, such as diabetes and Alzheimer's disease (AD), was rescued by overexpression of CERT, suggesting that CERT may control cellular ceramide levels through EV release (Bandet et al., 2018; Crivelli et al., 2021). Notably, Barman et al. discovered that downregulating VAP, which anchors CERT to the ER, not only reduces EV secretion but also a unique subset of RNA-containing EVs (Barman et al., 2022). This finding suggests a role of CERT in packaging of RNA in EVs as well.

These findings open-up new intervention strategies to control the number and ceramide content of EVs in disease condition. EVs have been proposed as the "Trojan horses of neurodegeneration" (Ghidoni et al., 2008). For instance, in AD, the release of amyloid-β (Aβ) peptides by EVs may be involved in the slow progression of the disease, similarly to prion proteins that mediate their intercellular transfer via EVs (Sardar Sinha et al., 2018). While great attention has been given to the protein and RNA cargo of EVs, the lipid composition of the EVs is poorly studied (Elsherbini & Bieberich, 2018). Our group showed that EVs enriched in ceramide contribute to Aβ aggregation and neurotoxicity in vitro and in the brain of AD mice models (Dinkins et al., 2014; Wang et al., 2012). Furthermore, reduction of ceramide generation by inhibition or genetic deficiency of N-SMase2 reduced EV formation and plaque numbers, and improved cognition in vivo in a transgenic model of AD (Dinkins et al., 2014, 2016). Therefore, investigation of drugs with the dual action of reducing EV numbers and reducing ceramide content in EVs could potentially give rise to new treatments for neurodegenerative diseases where ceramide-enriched EVs play a role. When administering HPA-12 intraperitoneally to mice for a week every other day, the number of EVs in brain and blood were not significantly affected. However, ceramide and SM were reduced in blood- and brain-derived EVs, respectively. Therefore, our study unravels a novel mechanism underlying the function of ceramide and CERT in EV biogenesis. This mechanism of N-SMase-2-independent, but Cer/CERT-dependent EV formation will also offer a novel pharmacological target to manipulate EV biogenesis and lipid composition, which is important for our understanding of the physiological and pathophysiological function of EVs and development of disease therapies.

5 | CONCLUSION

In conclusion, we report that CERT enters the endocytic pathway and is sorted to the MVE where a complex is formed between CERT and Tsg101, which is promoted by ceramide biosynthesis. CERT mediates a direct transport of ceramide between the ER and late endosomes/MVE at contact sites which determines the ceramide content of EVs. Translocation of ceramide-associated CERT to the MVE and biogenesis of EVs is potentially regulated by the interaction between the PH domain of CERT and PI4P generated by PI4KIIIβ in the Golgi apparatus or PI4KIIα in endosomes. Overexpression of CERT in neuronal cells increases EV secretion while inhibition of CERT with the drug HPA-12 reduces EV formation and the concentration of ceramide and SM in EVs. Our data support a novel function of CERT in regulating the biogenesis and sphingolipid composition of EVs, which links ceramide to the ESCRT-dependent pathway.

DISCLOSURE STATEMENT
The authors declare that they have no competing interests.

AUTHOR CONTRIBUTION
Erhard Bieberich, Simone M. Crivelli and Pilar Martinez-Martinez conceived the project and designed the experiments. Simone M. Crivelli with Erhard Bieberich performed the microscope experiments. Simone M. Crivelli, Ahmed Elsherbini and Zainud-din Quadri performed EV isolation and characterization. Zhihui Zhu cloned the GFP-tagged plasmids. Simone M. Crivelli and Priyanka Tripathi performed Western blotting. Simone M. Crivelli and Liping Zhang contributed to the production of primary neurons and the in vivo experiments. Dusan Berkes and Branislav Ferko synthetized HPA-12, NDB-HPA-12 and pacHPA-12. SDS, Simone M. Crivelli and Erhard Bieberich contributed to the analysis and interpretation of lipid measurements. Pilar Martinez-Martinez and Caterina Giovagnoni contributed with two hybrid system data. Jian Pu contributed with sample preparation for TEM. Simone M. Crivelli and Erhard Bieberich wrote the manuscript. All authors contributed by critically revising the manuscript.

ORCID

Simone M. Crivelli 🄳 https://orcid.org/0000-0003-1776-7761

REFERENCES

Andreu, Z. (2014). Tetraspanins in extracellular vesicle formation and function. *Frontiers in Immunology*, 5, 442.

Bandet, C. L., Mahfouz, R., Véret, J., Sotiropoulos, A., Poirier, M., Giussani, P., Campana, M., Philippe, E., Blachnio-Zabielska, A., Ballaire, R., Le Liepvre, X., Bourron, O., Berkeš, D., Górski, J., Ferré, P., Le Stunff, H., Foufelle, F., & Hajduch, E. (2018). Ceramide transporter CERT is involved in muscle insulin signaling defects under lipotoxic conditions. *Diabetes*, 67(7), 1258–1271.

Barman, B., Sung, B. H., Krystofiak, E., Ping, J., Ramirez, M., Millis, B., Allen, R., Prasad, N., Chetyrkin, S., Calcutt, M. W., Vickers, K., Patton, J. G., Liu, Q. i., & Weaver, A. M. (2022). VAP-A and its binding partner CERT drive biogenesis of RNA-containing extracellular vesicles at ER membrane contact sites. *Developmental Cell*, 57(8), 974–994.e8.

Bartel, P., Chien, C. T., Sternglanz, R., & Fields, S. (1993). Elimination of false positives that arise in using the two-hybrid system. *Biotechniques*, 14(6), 920–924.

Beranger, F. (1997). Getting more from the two-hybrid system: N-terminal fusions to LexA are efficient and sensitive baits for two-hybrid studies. *Nucleic Acids Research*, 25(10), 2035–2036.

Berkeš, D., Daïch, A., Santos, C., Ballereau, S., & Génisson, Y. (2016). Chemistry and biology of HPAs: A family of ceramide trafficking inhibitors. *Chemistry*, 22(49), 17514–17525.

Bielawski, J., Pierce, J. S., Snider, J., Rembiesa, B., Szulc, Z. M., & Bielawska, A. (2009). Comprehensive quantitative analysis of bioactive sphingolipids by high-performance liquid chromatography-tandem mass spectrometry. *Methods in Molecular Biology*, 579, 443–467.

Bielawski, J., Pierce, J. S., Snider, J., Rembiesa, B., Szulc, Z. M., & Bielawska, A. (2010). Sphingolipid analysis by high performance liquid chromatography-tandem mass spectrometry (HPLC-MS/MS). *Advances in Experimental Medicine and Biology*, 688, 46–59.

Crivelli, S. M., Luo, Q., Stevens, JoA. A., Giovagnoni, C., Van Kruining, D., Bode, G., Den Hoedt, S., Hobo, B., Scheithauer, A. -. L., Walter, J., Mulder, M. T., Exley, C., Mold, M., Mielke, M. M., De Vries, H. E., Wouters, K., Van Den Hove, D. L. A., Berkes, D., Ledesma, M. D., …, Martinez-Martinez, P. (2021). CERTL reduces C16 ceramide, amyloid-beta levels, and inflammation in a model of Alzheimer's disease. *Alzheimer's Research & Therapy*, 13(1), 45.

Crivelli, S. M., Paulus, A., Markus, J., Bauwens, M., Berkes, D., De Vries, H. E., Mulder, M. T., Walter, J., Mottaghy, F. M., Losen, M., & Martinez-Martinez, P. (2017). Synthesis, radiosynthesis, and preliminary in vitro and in vivo evaluation of the fluorinated ceramide trafficking inhibitor (HPA-12) for brain applications. *Journal of Alzheimer's Disease*, 60(3), 783–794.

Crivelli, S. M., Van Kruining, D., Luo, Q., Stevens, JoA. A., Giovagnoni, C., Paulus, A., Bauwens, M., Berkes, D., De Vries, H. E., Mulder, M. T., Walter, J., Waelkens, E., Derua, R., Swinnen, J. V., Dehairs, J., Mottaghy, F. M., Losen, M., Bieberich, E., & Martinez-Martinez, P. (2020). Ceramide analog [18F]F-HPA-12 detects sphingolipid disbalance in the brain of Alzheimer's disease transgenic mice by functioning as a metabolic probe. *Scientific Reports*, 10(1), 19354.

De Matteis, M. A., & D'Angelo, G. The role of the phosphoinositides at the Golgi complex. *Biochemical Society Symposia*, 2007(74), 107–116.

De Matteis, M. A., Wilson, C., & D'angelo, G. (2013). Phosphatidylinositol-4-phosphate: The Golgi and beyond. *Bioessays*, 35(7), 612–622.

Dichlberger, A., Zhou, K., Bäck, N., Nyholm, T., Backman, A., Mattjus, P., Ikonen, E., & Blom, T. (2021). LAPTM4B controls the sphingolipid and ether lipid signature of small extracellular vesicles. *Biochimica et Biophysica Acta - Molecular and Cell Biology of Lipids*, 1866(2), 158855.

Dinkins, M. B., Dasgupta, S., Wang, G., Zhu, G. u., & Bieberich, E. (2014). Exosome reduction in vivo is associated with lower amyloid plaque load in the 5XFAD mouse model of Alzheimer's disease. *Neurobiology of Aging*, 35(8), 1792–1800.

Dinkins, M. B., Enasko, J., Hernandez, C., Wang, G., Kong, J., Helwa, I., Liu, Y., Terry, A. V., & Bieberich, E. (2016). Neutral sphingomyelinase-2 deficiency ameliorates Alzheimer's disease pathology and improves cognition in the 5XFAD mouse. *Journal of Neuroscience*, 36(33), 8653–8667.

Elsherbini, A., & Bieberich, E. (2018). Ceramide and exosomes: A novel target in cancer biology and therapy. *Advances in Cancer Research*, 140, 121–154.

Elsherbini, A., Kirov, A. S., Dinkins, M. B., Wang, G., Qin, H., Zhu, Z., Tripathi, P., Crivelli, S. M., & Bieberich, E. (2020). Association of Abeta with ceramide-enriched astrosomes mediates Abeta neurotoxicity. *Acta Neuropathologica Communications*, 8(1), 60.

Formstecher, E., Aresta, S., Collura, V., Hamburger, A., Meil, A., Trehin, A., Reverdy, C., Betin, V., Maire, S., Brun, C., Jacq, B., Arpin, M., Bellaiche, Y., Bellusci, S., Benaroch, P., Bornens, M., Chanet, R., Chavrier, P., Delattre, O., & …, Daviet, L. (2005). Protein interaction mapping: A Drosophila case study. *Genome Research*, 15(3), 376–384.

Fukushima, M., Dasgupta, D., Mauer, A. S., Kakazu, E., Nakao, K., & Malhi, H. (2018). StAR-related lipid transfer domain 11 (STARD11)-mediated ceramide transport mediates extracellular vesicle biogenesis. *Journal of Biological Chemistry*, 293(39), 15277–15289.

Gad, S. C., Cassidy, C. D., Aubert, N., Spainhour, B., & Robbe, H. (2006). Nonclinical vehicle use in studies by multiple routes in multiple species. *International Journal of Toxicology*, 25(6), 499–521.

Gault, C. R., Obeid, L. M., & Hannun, Y. A. (2010). An overview of sphingolipid metabolism: From synthesis to breakdown. *Advances in Experimental Medicine and Biology*, 688, 1–23.

Ghidoni, R., Benussi, L., & Binetti, G. (2008). Exosomes: The Trojan horses of neurodegeneration. *Medical Hypotheses*, 70(6), 1226–1227.

Hanada, K., Kumagai, K., Yasuda, S., Miura, Y., Kawano, M., Fukasawa, M., & Nishijima, M. (2003). Molecular machinery for non-vesicular trafficking of ceramide. *Nature*, 426(6968), 803–809.

Henmi, Y., Morikawa, Y., Oe, N., Ikeda, N., Fujita, A., Takei, K., Minogue, S., & Tanabe, K. (2016). PtdIns4KIIalpha generates endosomal PtdIns(4)P and is required for receptor sorting at early endosomes. *Molecular Biology of the Cell*, 27(6), 990–1001.

Jiang, X., Zhu, Z., Qin, H., Tripathi, P., Zhong, L., Elsherbini, A., Karki, S., Crivelli, S. M., Zhi, W., Wang, G., Spassieva, S. D., & Bieberich, E. (2019). Visualization of ceramide-associated proteins in ceramide-rich platforms using a cross-linkable ceramide analog and proximity ligation assays with anti-ceramide antibody. *Frontiers in Cell and Developmental Biology*, 7, 166.

Kabani, M., Boisramé, A., Beckerich, J. -. M., & Gaillardin, C. (2000). A highly representative two-hybrid genomic library for the yeast Yarrowia lipolytica. *Gene*, 241(2), 309–315.

Kawano, M., Kumagai, K., Nishijima, M., & Hanada, K. (2006). Efficient trafficking of ceramide from the endoplasmic reticulum to the Golgi apparatus requires a VAMP-associated protein-interacting FFAT motif of CERT. *Journal of Biological Chemistry*, 281(40), 30279–30288.

Kenific, C. M., Zhang, H., & Lyden, D. (2021). An exosome pathway without an ESCRT. *Cell Research*, 31(2), 105–106.

Kumagai, K., & Hanada, K. (2019). Structure, functions and regulation of CERT, a lipid-transfer protein for the delivery of ceramide at the ER-Golgi membrane contact sites. *Febs Letters*, 593(17), 2366–2377.

Kumagai, K., Yasuda, S., Okemoto, K., Nishijima, M., Kobayashi, S., & Hanada, K. (2005). CERT mediates intermembrane transfer of various molecular species of ceramides. *Journal of Biological Chemistry*, 280(8), 6488–6495.

Mencarelli, C., Losen, M., Hammels, C., De Vry, J., Hesselink, M. K. C., Steinbusch, H. W. M., De Baets, M. H., & Martínez-Martínez, P. (2010). The ceramide transporter and the Goodpasture antigen binding protein: One protein–one function? *Journal of Neurochemistry*, *113*(6), 1369–1386.

Mencarelli, C., Bode, G. H., Losen, M., Kulharia, M., Molenaar, P. C., Veerhuis, R., Steinbusch, H. W. M., De Baets, M. H., Nicolaes, G. A. F., & Martinez-Martinez, P. (2012). Goodpasture antigen-binding protein/ceramide transporter binds to human serum amyloid P-component and is present in brain amyloid plaques. *Journal of Biological Chemistry*, *287*(18), 14897–14911.

Menck, K., Sönmezer, C., Worst, T. S., Schulz, M., Dihazi, G. H., Streit, F., Erdmann, G., Kling, S., Boutros, M., Binder, C., & Gross, J. C. (2017). Neutral sphingomyelinases control extracellular vesicles budding from the plasma membrane. *Journal Of Extracellular Vesicles*, *6*(1), 1378056.

Minciacchi, V. R., Freeman, M. R., & Di Vizio, D. (2015). Extracellular vesicles in cancer: Exosomes, microvesicles and the emerging role of large oncosomes. *Seminars in Cell & Developmental Biology*, *40*, 41–51.

Mirdita, M., Ovchinnikov, S., & Steinegger, M. (2021). ColabFold - Making protein folding accessible to all. 2021.08.15.456425.

Nagano, M., Toshima, J. Y., Siekhaus, D. E., & Toshima, J. (2019). Rab5-mediated endosome formation is regulated at the trans-Golgi network. Communications Biology, (2), 419. https://doi.org/10.1038/s42003-019-0670-5

Perez-Gonzalez, R., Gauthier, S. A., Kumar, A., Saito, M., Saito, M., & Levy, E. (2017). A method for isolation of extracellular vesicles and characterization of exosomes from brain extracellular space. *Methods in Molecular Biology*, *1545*, 139–151.

Perez-Hernandez, D., Gutiérrez-Vázquez, C., Jorge, I., López-Martín, S., Ursa, A., Sánchez-Madrid, F., Vázquez, J., & Yáñez-Mó, M. (2013). The intracellular interactome of tetraspanin-enriched microdomains reveals their function as sorting machineries toward exosomes. *Journal of Biological Chemistry*, *288*(17), 11649–11661.

Pettersen, E. F., Goddard, T. D., Huang, C. C., Meng, E. C., Couch, G. S., Croll, T. I., Morris, J. H., & Ferrin, T. E. (2021). UCSF ChimeraX: Structure visualization for researchers, educators, and developers. *Protein Science*, *30*(1), 70–82.

Prashek, J., Truong, T., & Yao, X. (2013). Crystal structure of the pleckstrin homology domain from the ceramide transfer protein: Implications for conformational change upon ligand binding. *Plos One*, *8*(11), e79590.

Raiborg, C., Wenzel, E. M., & Stenmark, H. (2015). ER-endosome contact sites: Molecular compositions and functions. *Embo Journal*, *34*(14), 1848–1858.

Rao, R. P., Scheffer, L., Srideshikan, S. M., Parthibane, V., Kosakowska-Cholody, T., Masood, M. A., Nagashima, K., Gudla, P., Lockett, S., Acharya, U., & Acharya, J. K. (2014). Ceramide transfer protein deficiency compromises organelle function and leads to senescence in primary cells. *Plos One*, *9*(3), e92142.

Rao, R. P., Yuan, C., Allegood, J. C., Rawat, S. S., Edwards, M. B., Wang, X., Merrill, A. H., Acharya, U., & Acharya, J. K. (2007). Ceramide transfer protein function is essential for normal oxidative stress response and lifespan. *Proceedings of the National Academy of Sciences of the United States of America*, *104*(27), 11364–11369.

Rutaganira, F. U., Fowler, M. L., Mcphail, J. A., Gelman, M. A., Nguyen, K., Xiong, A., Dornan, G. L., Tavshanjian, B., Glenn, J. S., Shokat, K. M., & Burke, J. E. (2016). Design and structural characterization of potent and selective inhibitors of phosphatidylinositol 4 kinase IIIbeta. *Journal of Medicinal Chemistry*, *59*(5), 1830–1839.

Santos, C., Fleury, L., Rodriguez, F., Markus, J., Berkeš, D., Daïch, A., Ausseil, F., Baudoin-Dehoux, C., Ballereau, S., & Génisson, Y. (2015). The CERT antagonist HPA-12: First practical synthesis and individual binding evaluation of the four stereoisomers. *Bioorganic & Medicinal Chemistry*, *23*(9), 2004–2009.

Santos, C., Rogriguez, F., Garcia, V., Moravčíková, D., Berkeš, D., Daïch, A., Levade, T., Baudoin-Dehoux, C., Ballereau, S., & Génisson, Y. (2014). Identification of novel CERT ligands as potential ceramide trafficking inhibitors. *Chembiochem*, *15*(17), 2522–2528.

Sardar Sinha, M., Ansell-Schultz, A., Civitelli, L., Hildesjö, C., Larsson, M., Lannfelt, L., Ingelsson, M., & Hallbeck, M. (2018). Alzheimer's disease pathology propagation by exosomes containing toxic amyloid-beta oligomers. *Acta Neuropathologica*, *136*(1), 41–56.

Sengupta, N., Jović, M., Barnaeva, E., Kim, D. W., Hu, X., Southall, N., Dejmek, M., Mejdrova, I., Nencka, R., Baumlova, A., Chalupska, D., Boura, E., Ferrer, M., Marugan, J., & Balla, T. (2019). A large scale high-throughput screen identifies chemical inhibitors of phosphatidylinositol 4-kinase type II alpha. *Journal of Lipid Research*, *60*(3), 683–693.

Skotland, T., Hessvik, N. P., Sandvig, K., & Llorente, A. (2019). Exosomal lipid composition and the role of ether lipids and phosphoinositides in exosome biology. *Journal of Lipid Research*, *60*(1), 9–18.

Soares Martins, T., Trindade, D., Vaz, M., Campelo, I., Almeida, M., Trigo, G., Da Cruz E Silva, O. A. B., & Henriques, A. G. (2021). Diagnostic and therapeutic potential of exosomes in Alzheimer's disease. *Journal of Neurochemistry*, *156*(2), 162–181.

Sugiki, T., Takeuchi, K., Yamaji, T., Takano, T., Tokunaga, Y., Kumagai, K., Hanada, K., Takahashi, H., & Shimada, I. (2012). Structural basis for the Golgi association by the pleckstrin homology domain of the ceramide trafficking protein (CERT). *Journal of Biological Chemistry*, *287*(40), 33706–33718.

Tao-Cheng, J. -. H., Crocker, V., Moreira, S. L., & Azzam, R. (2021). Optimization of protocols for pre-embedding immunogold electron microscopy of neurons in cell cultures and brains. *Molecular Brain*, *14*(1), 86.

Trajkovic, K., Hsu, C., Chiantia, S., Rajendran, L., Wenzel, D., Wieland, F., Schwille, P., BrüGger, B., & Simons, M. (2008). Ceramide triggers budding of exosome vesicles into multivesicular endosomes. *Science*, *319*(5867), 1244–1247.

Vojtek, A. B., & Hollenberg, S. M. (1995). Ras-Raf interaction: Two-hybrid analysis. *Methods in Enzymology*, *255*, 331–342.

Wang, G., Dinkins, M., He, Q., Zhu, G. u., Poirier, C., Campbell, A., Mayer-Proschel, M., & Bieberich, E. (2012). Astrocytes secrete exosomes enriched with proapoptotic ceramide and prostate apoptosis response 4 (PAR-4): Potential mechanism of apoptosis induction in Alzheimer disease (AD). *Journal of Biological Chemistry*, *287*(25), 21384–21395.

Wilhelm, L. P., Wendling, C., Védie, B., Kobayashi, T., Chenard, M. -. P., Tomasetto, C., Drin, G., & Alpy, F. (2017). STARD3 mediates endoplasmic reticulum-to-endosome cholesterol transport at membrane contact sites. *Embo Journal*, *36*(10), 1412–1433.

Willms, E., Johansson, H. J., Mäger, I., Lee, Y. i., Blomberg, K. E. M., Sadik, M., Alaarg, A., Smith, C. I. E., Lehtiö, J., El Andaloussi, S., Wood, M. J. A., & Vader, P. (2016). Cells release subpopulations of exosomes with distinct molecular and biological properties. *Scientific Reports*, *6*(1), 22519.

Yamaji, T., & Hanada, K. (2014). Establishment of HeLa cell mutants deficient in sphingolipid-related genes using TALENs. *Plos One*, *9*(2), e88124.

Yasuda, S., Kitagawa, H., Ueno, M., Ishitani, H., Fukasawa, M., Nishijima, M., Kobayashi, S., & Hanada, K. (2001). A novel inhibitor of ceramide trafficking from the endoplasmic reticulum to the site of sphingomyelin synthesis. *Journal of Biological Chemistry*, *276*(47), 43994–44002.

Yoshida, A., Hayashi, H., Tanabe, K., & Fujita, A. (2017). Segregation of phosphatidylinositol 4-phosphate and phosphatidylinositol 4,5-bisphosphate into distinct microdomains on the endosome membrane. *Biochimica et Biophysica Acta*, *1859*(10), 1880–1890.

Yuyama, K., Sun, H., Mitsutake, S., & Igarashi, Y. (2012). Sphingolipid-modulated exosome secretion promotes clearance of amyloid-beta by microglia. *Journal of Biological Chemistry*, *287*(14), 10977–10989.

SUPPORTING INFORMATION

Additional supporting information can be found online in the Supporting Information section at the end of this article.